Indirect and Direct Impacts of Typhoon In-Fa (2021) on Heavy Precipitation in Inland and Coastal Areas of China: Synoptic-Scale Environments and Return Period Analysis

LIANGYI WANG,[a,b] XIHUI GU,[a,c,d,e,f,g] LOUISE J. SLATER,[h] YANGCHEN LAI,[b] XIANG ZHANG,[i] DONGDONG KONG,[a,e] JIANYU LIU,[j] AND JIANFENG LI[b]

[a] *Department of Atmospheric Science, School of Environmental Studies, China University of Geosciences, Wuhan, China*
[b] *Department of Geography, Hong Kong Baptist University, Hong Kong, China*
[c] *State Key Laboratory of Water Resources and Hydropower Engineering Science, Wuhan University, Wuhan, China*
[d] *SongShan Laboratory, Zhengzhou, China*
[e] *Centre for Severe Weather and Climate and Hydro-geological Hazards, Wuhan, China*
[f] *Hubei Key Laboratory of Yangtze Catchment Environmental Aquatic Science, School of Environmental Studies, China University of Geosciences, Wuhan, China*
[g] *State Environmental Protection Key Laboratory of Source Apportionment and Control of Aquatic Pollution, Ministry of Ecology and Environment, Wuhan, China*
[h] *School of Geography and the Environment, University of Oxford, Oxford, United Kingdom*
[i] *National Engineering Research Center of Geographic Information System, School of Geography and Information Engineering, China University of Geosciences, Wuhan, China*
[j] *Hubei Key Laboratory of Critical Zone Evolution, School of Geography and Information Engineering, China University of Geosciences, Wuhan, China*

(Manuscript received 15 August 2022, in final form 18 May 2023, accepted 7 June 2023)

ABSTRACT: In July 2021, Typhoon In-Fa (TIF) triggered a significant indirect heavy precipitation event (HPE) in central China and a direct HPE in eastern China. Both these events led to severe disasters. However, the synoptic-scale conditions and the impacts of these HPEs on future estimations of return periods remain poorly understood. Here, we find that the remote HPE that occurred ~2200 km ahead of TIF over central China was a predecessor rain event (PRE). The PRE unfolded under the equatorward entrance of the upper-level westerly jet. This event, which encouraged divergent and adiabatic outflow in the upper level, subsequently intensified the strength of the upper-level westerly jet. In contrast, the direct HPE in eastern China was due primarily to the long duration and slow movement of TIF. The direct HPE occurred in areas situated less than 200 km from TIF's center and to the left of TIF's propagation trajectory. Anomaly analyses reveal favorable thermodynamic and dynamic conditions and abundant atmospheric moisture that sustained TIF's intensity. A saddle-shaped pressure field in the north of eastern China and peripheral weak steering flow impeded TIF's movement northward. Hydrologically, the inclusion of these two HPEs in the historical record leads to a decrease in the estimated return periods of similar HPEs. Our findings highlight the potential difficulties that HPEs could introduce for the design of hydraulic engineering infrastructure as well as for the disaster mitigation measures required to alleviate future risk, particularly in central China.

KEYWORDS: Tropical cyclones; Climate change; Hydrology

1. Introduction

From the genesis to the demise of Typhoon In-Fa (TIF; 17–31 July 2021), heavy precipitation events (HPEs) occurred in the central (mainly Henan) and eastern (mainly Jiangsu and Zhejiang) provinces of China. During 19–21 July, while TIF was located in the western North Pacific (WNP), TIF remotely triggered an indirect HPE situated more than 1000 km away from its center, in central China. Subsequently, during 22–28 July, a direct HPE occurred in eastern China along TIF's eyewall, inner and outer spiral rainbands, within 100 km of its center. Both the indirect and direct HPEs were rare and caused catastrophic losses (Fu et al. 2022). For example, the most extreme hourly precipitation during TIF in central China was 201.9 mm, exceeding the hourly precipitation recorded by meteorological observation stations over the mainland of China since the establishment of these stations; similarly, the highest total precipitation directly caused by TIF in eastern China was above 1034 mm and also record-breaking (Fu et al. 2022; W. Li et al. 2022). Understanding the synoptic-scale environments and hydrological impacts (i.e., return period analysis) of the HPEs indirectly and directly induced by TIF is important to explain the physical mechanisms and highlight the importance of mitigating the damages of such extreme events.

Compared to the direct TIF-induced HPE in eastern China, the socioeconomic losses of the indirect TIF-induced HPE in central China were more deadly (i.e., 302 deaths and direct property losses of more than 88.5 billion Chinese yuan, which

Supplemental information related to this paper is available at the Journals Online website: https://doi.org/10.1175/MWR-D-22-0241.s1.

Corresponding authors: Xihui Gu, guxh@cug.edu.cn; Jianfeng Li, jianfengli@hkbu.edu.hk

DOI: 10.1175/MWR-D-22-0241.1

© 2023 American Meteorological Society. This published article is licensed under the terms of the default AMS reuse license. For information regarding reuse of this content and general copyright information, consult the AMS Copyright Policy (www.ametsoc.org/PUBSReuseLicenses).

Brought to you by UNIVERSITY OF OXFORD-RADCLIFFE | Unauthenticated | Downloaded 09/18/23 11:06 AM UTC

represents around $13.67 billion (U.S. dollars) and EUR 11.56 billion). Given the catastrophic losses, it is imperative to explore the possible mechanisms of the indirect TIF-induced HPE (Cheng et al. 2022; Yang et al. 2022; Yin et al. 2022; Zhao et al. 2022). For example, Yin et al. (2022) indicated that within the convective system, the combination of cloud microphysics and horizontal transportation enabled by the vertically rising and converging zone facilitated the rapid accumulation and settling of a substantial amount of water vapor. This in turn precipitated the HPE in central China. Using the moisture budget equation, Cheng et al. (2022) found that 75% and 22% of the HPE in central China was explained by dynamic and thermodynamic factors. However, these studies mostly focused on the large-scale circulation mechanisms of the HPEs, ignoring how TIF remotely triggered the HPE in central China.

Some HPEs distantly induced by tropical cyclones (TCs) have been reported in the past and they are usually described as predecessor rain events (PREs; Galarneau et al. 2010; Bosart et al. 2012; Moore 2010; Moore et al. 2013; Baek et al. 2015; Yuan et al. 2018). For example, Galarneau et al. (2010) found that record-breaking PREs of >250 mm within 24 h induced by Hurricane Erin (2007) were situated ~1200 km poleward of Erin (i.e., over Minnesota and Lake Michigan of the United States). Yuan et al. (2018) detected that 19% of TCs generated in the Bay of Bengal during 1981–2012 led to PREs in the southeast Yunnan province of China. Cote (2007) defined a PRE as a coherent area of heavy precipitation, with 24-h accumulated precipitation exceeding 100 mm, located more than 1000 km poleward of a landfalling TC, and physically separated from the main precipitation belts directly induced by the TC. TC-induced PREs can trigger devastating floods and economic losses (Galarneau et al. 2010), and therefore, there is an urgent need to carefully consider PREs and their impacts. However, important research questions remain: was the indirect TIF-induced HPE in central China a PRE, and if so, how did TIF remotely trigger this PRE?

The region of eastern China, which was close to TIF's center and directly influenced by TIF, experienced more extreme precipitation due to the record-breaking duration of TIF over land (W. Li et al. 2022; Yang et al. 2022; Wu et al. 2022). Some studies have analyzed some of the circulation features of the HPE directly induced by TIF in eastern China. For instance, the weak steering flow led by the large-scale environment and the long persistence of TIF's circulation were the two most important background conditions explaining the extreme duration of the HPE in eastern China (Yang et al. 2022). Nevertheless, it is still unclear which physical mechanisms contributed to the record-breaking process precipitation event in eastern China, and can explain both the long duration and the slow movement of TIF as it made landfall.

Both HPEs, whether indirectly or directly induced by TIF, triggered heavy urban floods and stormwater, causing economic losses and casualties (Chan et al. 2022; Wang et al. 2022). To prevent or decrease the losses from HPEs and associated floods, hydraulic engineering infrastructure (such as open channels and pipes) is constructed using specific design standards, which normally refer to return periods which are estimated by using the generalized extreme value distribution based on historical HPE and/or flood time series (Mirhosseini et al. 2013; Zeng at al. 2019; Aiyelokun et al. 2021). Extreme precipitation frequency analysis is an essential basis for estimating the return periods required for the design of such infrastructure. The upper-tail behavior of the frequency curve determines the accuracy of return period estimates for rare events (Gu et al. 2017; Ben Alaya et al. 2020; Quesada-Román et al. 2022). Past studies have shown that TCs play an important role in the shape of extreme precipitation frequency curves and their upper-tail features (Risser and Wehner 2017; Gu et al. 2017; Zhou et al. 2018). For example, the East Asian coasts and southeastern American coasts show common heavy tail characteristics of extreme precipitation frequency curves due to the impacts of landfalling TCs (Cavanaugh et al. 2015). Combined with synoptic-scale environment analysis, investigating the impacts of indirect and direct TIF-induced HEPs on local return period (i.e., precipitation frequency) estimations can provide important scientific information for water disaster management institutions to enhance risk mitigation measures.

In this study, we first describe the spatiotemporal evolution of the two HPEs indirectly and directly induced by TIF, then explore the synoptic-scale environments during TIF for both HPEs in central and eastern China, and finally analyze how the TIF-induced HPEs affect local return period estimation of precipitation extremes.

2. Data and methods

a. *Precipitation data and typhoon data*

Observed station-based hourly precipitation at 2481 stations and gridded daily precipitation at 0.5° resolution during 1961–2021 were collected from the China Meteorological Data Service Center (http://www.nmic.cn/en). Hourly global real-time satellite precipitation with high spatial resolution (i.e., 4 km × 4 km) from 2003 to the present was developed by the Center for Hydrometeorology and Remote Sensing at the University of California (https://chrsdata.eng.uci.edu/).

Typhoon data covering the WNP during 1961–2021 were obtained from the International Best Track Archive for Climate Stewardship (IBTrACS; https://www.ncdc.noaa.gov/ibtracs/; Knapp et al. 2010, 2018). TIF track was downloaded from the Department of Water Resources of Zhejiang Province (http://typhoon.zjwater.gov.cn/default.aspx).

b. *ERA5 data*

Large-scale environmental variables during 1961–2021 were obtained from the European Centre for Medium-Range Weather Forecasts Re-Analysis 5 (ERA5; https://www.ecmwf.int/en/forecasts/datasets/reanalysis-datasets/era5; Hersbach et al. 2018a,b) dataset. The ERA5 dataset has a 0.25° × 0.25° spatial resolution and hourly temporal resolution. All 2D and 3D variables presented in subsequent analyses are taken from ERA5.

c. *Generalized extreme value distribution*

Extreme value frequency analysis based on the generalized extreme value (GEV) distribution is typically employed to

Brought to you by UNIVERSITY OF OXFORD-RADCLIFFE | Unauthenticated | Downloaded 09/18/23 11:06 AM UTC

estimate return periods of hydrometeorological variables (e.g., heavy precipitation and flood peaks; Vasiliades et al. 2015; Fowler and Kilsby 2003). Here, we conduct heavy precipitation frequency analysis using the GEV distribution (Schaller et al. 2016; Gu et al. 2017; Yang et al. 2019):

$$F(x|\mu, \sigma, \xi) = \exp\left\{-\left[1 + \xi\left(\frac{x-\mu}{\sigma}\right)\right]^{-1/\xi}\right\}, \quad (1)$$

where μ, σ, and ξ represent location, scale, and shape parameters, respectively. The location and scale parameters (i.e., μ and σ) are connected with precipitation magnitude and variability, respectively. The shape parameter (i.e., ξ) dominates the upper tail of the heavy precipitation frequency curve. Positive and negative ξ values represent thick and light upper tails of the heavy precipitation frequency distribution, respectively. The return period estimation of rare events largely depends on the upper tail (i.e., shape parameter).

d. *Extreme precipitation ratio and relative percent difference based on return period*

A HPE is defined as the maximum 1- and 5-day accumulated precipitation per year (Rx1day and Rx5day), and is area averaged over the study regions (i.e., central China and eastern China, respectively). We use the GEV distribution to compute the 10-yr precipitation peak from the annual precipitation series (i.e., Rx1day and Rx5day) over the period of 1961–2021, i.e., the precipitation peak that occurs, on average, once in 10 years and

TABLE 1. List of abbreviations used in this study.

Full name	Abbreviation
Typhoon In-Fa	TIF
Heavy precipitation event	HPE
Predecessor rain event	PRE
Western North Pacific	WNP
Tropical cyclone	TC
International Best Track Archive for Climate Stewardship	IBTrACS
European Centre for Medium-Range Weather Forecasts Re-Analysis 5	ERA5
Generalized extreme value	GEV
Max 1-day accumulated precipitation	Rx1day
Max 5-day accumulated precipitation	Rx5day
Extreme precipitation ratio	EPR
Relative percent difference	RPD
Western Pacific subtropical high	WPSH

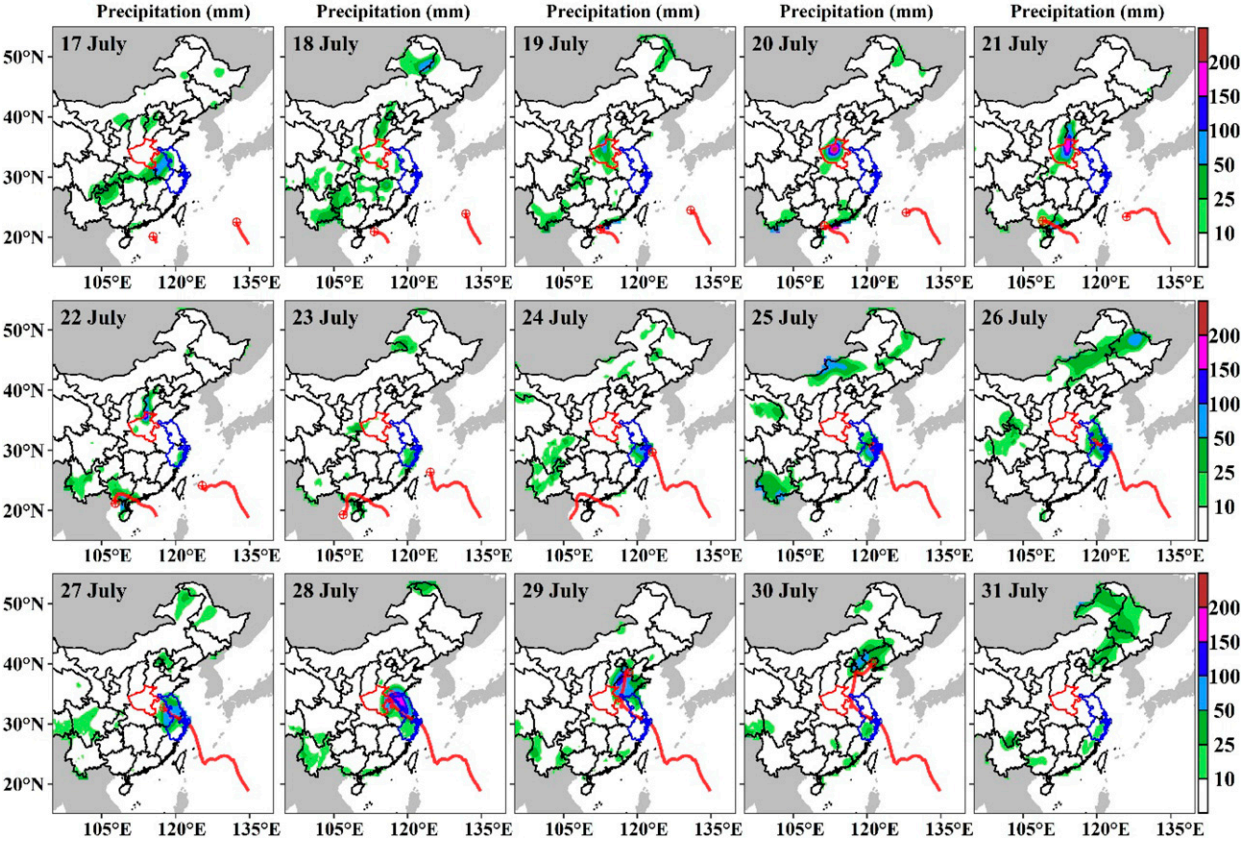

FIG. 1. Maps of observed gridded daily precipitation during Typhoon In-Fa (TIF; 17–31 Jul 2021). The red curves indicate the best tracks of TIF (in eastern China) and Typhoon Cempaka (in southern China). The red polygon in each panel represents the Henan province of China. The blue polygon in each panel represents the Jiangsu and Zhejiang provinces of China.

Brought to you by UNIVERSITY OF OXFORD-RADCLIFFE | Unauthenticated | Downloaded 09/18/23 11:06 AM UTC

is appropriate for the examination of extreme events (Ntegeka and Willems 2008; Stevenson and Schumacher 2014). Given the strong connection between precipitation properties and geographic regions, it is important to normalize the HPEs by their local 10-yr precipitation peak (i.e., the extreme precipitation ratio, EPR), providing a regional view of the HPEs during TIF (Czajkowski et al. 2013; Villarini et al. 2014; Yang et al. 2020). The EPR evaluates how much larger than the 10-yr precipitation peak the TIF-induced HPEs were. When EPR values are larger or smaller than 1, it suggests that the HPEs caused by TIF were larger or smaller than the 10-yr precipitation peak.

An additional heavy precipitation frequency analysis is conducted to explore TIF's impact on return period estimates. Barth et al. (2017) used the estimated magnitudes of the given annual exceedance probabilities [i.e., the reciprocals of return periods; de Lange and Gibb (2000), O'Connell (2005), Cooley (2012), Jenkins et al. (2012), Osetinsky-Tzidaki and Fredj (2022)] from all flood peaks and from atmospheric river-induced flood peaks to compute the relative percent difference (RPD). In this study, the relative percent difference (RPD) between the estimated magnitudes of the given return periods from Rx1day and Rx5day records, with and without the TIF-induced HPEs, for each given station, is calculated:

$$\mathrm{RPD} = \frac{M_{\mathrm{Entire}} - M_{\mathrm{No-TIF}}}{M_{\mathrm{Entire}}} \times 100\%, \qquad (2)$$

where M_{Entire} and $M_{\mathrm{No-TIF}}$ represent the Rx1day and Rx5day estimated with and without inclusion of TIF under the given return periods (i.e., 10, 50, and 100 years), respectively. A positive or negative RPD value indicates a higher or lower GEV return period estimate from the entire precipitation series when including the TIF-induced HPE. For the convenience of reading, a list of the abbreviations used in the dataset is shown in Table 1.

Using the station-based and gridded precipitation data and typhoon track data, we show the spatial–temporal features of precipitation during TIF. Further, we explore the synoptic patterns of the indirect and direct HPEs in central and eastern China. From the perspective of PRE, we reveal the moisture configurations, lifting and frontogenesis, and upper-level jet during the indirect TIF-induced HPE. For the direct HPE in eastern China, using satellite precipitation and large-scale environmental variables from ERA5, we described the evolution of precipitation distribution as a function of distance (≤500 km) to TIF's center (i.e., Lagrangian approach) and explored the evolution of precipitation distribution near the TC. In addition, using large-scale environmental variables from ERA5, we conducted an anomaly analysis to analyze why the long duration of TIF occurred, and to explain the slow movement of TIF. Both HPEs in central and eastern China caused serious economic losses, infrastructure damage and casualties. Normally, hydraulic engineering infrastructures, which can prevent HPEs and associated floods and further losses, are designed based on return periods which are estimated by the GEV distribution; however, such HPEs may influence the GVE distribution and further change the return period estimations, influencing the prevention of future HPEs. Therefore, we explored the impact of TIF on return period estimations by using the GEV distribution, and included

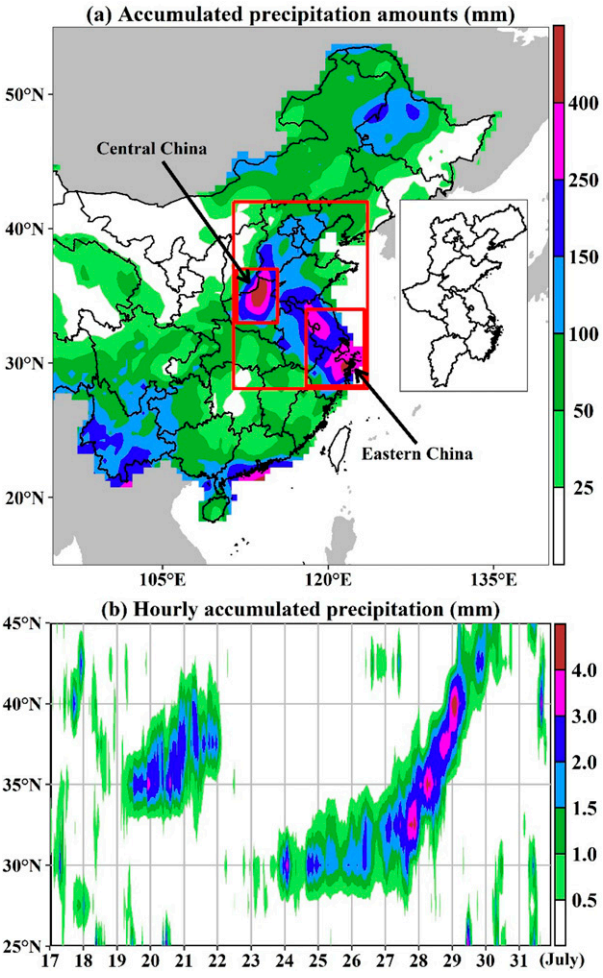

FIG. 2. (a) Accumulated precipitation amounts (based on observed gridded daily precipitation) and (b) latitude–temporal cross section of hourly accumulated precipitation (based on observed station-based hourly precipitation) during TIF (i.e., 17–31 Jul 2021). In (a) the large red box represents the region that experienced heavier precipitation. The black box to the right indicates the main provinces included in the large red box. The small red boxes indicate central China (on the left; 33°–37°N, 111.5°–115.5°E) and eastern China (on the right; 28°–34°N, 118°–123.5°E). In (b) hourly precipitation is averaged latitudinally based on the right black box in (a).

further EPR and RPD analyses also. The flowchart of this study is shown in Fig. S1 in the online supplemental material.

3. Results and discussion

a. Spatial–temporal features of the precipitation during TIF

We show the spatial distribution of daily precipitation in China during TIF in Fig. 1. While TIF was located over the WNP, a HPE in part of Henan province (i.e., central China) occurred on 19 July, peaked on 20 July (i.e., >150–400 mm), and receded in a northeasterly direction northeasterly on 21 July. The distance between the HPE in central China and TIF was approximately

Brought to you by UNIVERSITY OF OXFORD-RADCLIFFE | Unauthenticated | Downloaded 09/18/23 11:06 AM UTC

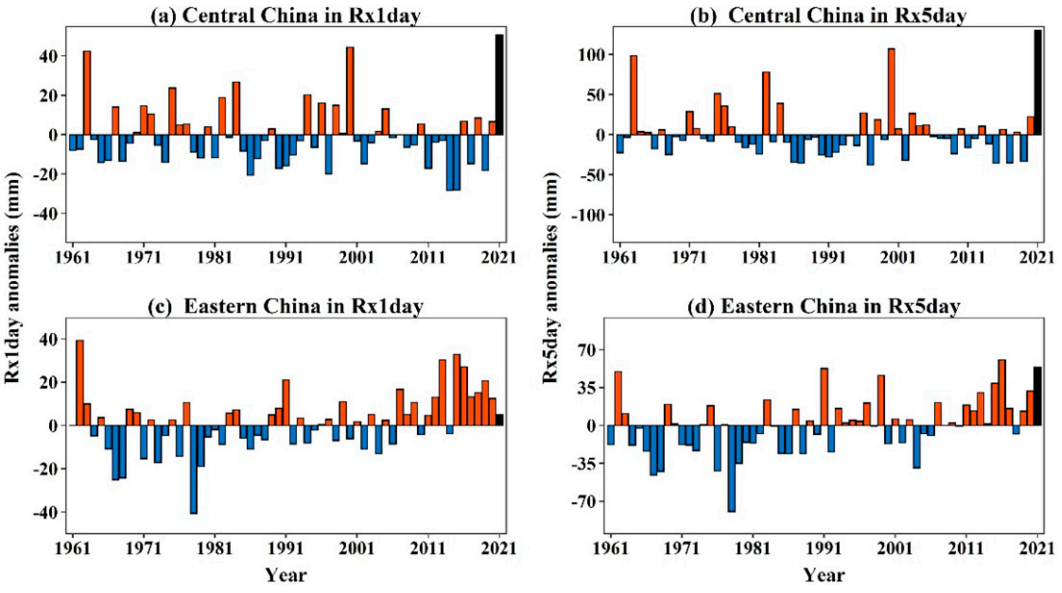

FIG. 3. Time series of regional average maximum 1- and 5-day accumulated precipitation (Rx1day and Rx5day; based on observed station-based hourly precipitation) anomalies during 1961–2021. The period 1981–2010 is used as the climatology to calculate the anomalies. The HPEs in 2021 are selected during the period of TIF (17–31 Jul 2021). The black bar in 2021 shows the HPE anomaly during TIF.

2200 km. In the South China Sea, another Typhoon, Cempaka, also appeared during 19–21 July. Over the period of 22–29 July, a HPE (i.e., >50–150 mm) appeared and developed in eastern China as TIF made landfall, and traveled over eastern China. It should be noted that the two HPEs in central China and eastern China are geographically divided, suggesting they were generated by different mechanisms.

For the accumulated precipitation (Fig. 2a), there were two main heavy precipitation regions: one was largely confined to central China (33°–37°N, 111.5°–115.5°E; left red box), and the other was largely confined to eastern China (28°–34°N, 118°–123.5°E; right red box). The two regions are consistent with the spatial distribution of heavy precipitation shown in Fig. 1. In central China, precipitation mainly occurred during 19–21 July, with a maximum accumulated precipitation amount exceeding 400 mm. Over the period of 22–29 July, there were two accumulated precipitation centers (one in the northwest of eastern China, and the other in the southeast), with accumulated precipitation amounts exceeding 250 mm.

From the perspective of the latitudinal–temporal evolution of hourly average precipitation (Fig. 2b), there were two clear precipitation phases. Phase 1 occurred during 19–21 July when the HPE region was along 35°N, reaching two precipitation peaks at 1600 UTC 20 July and 1000 UTC 21 July, respectively. Phase 2 was during 23–29 July when the precipitation center first appeared along 30°N and eventually moved northward to 40°N, which was associated with the landfall and northward movement of TIF. The distinct spatial–temporal separation between the two precipitation phases indicates the two HPEs during TIF were independent.

Considering that both of the two HPEs persisted over 3–5 days, we focus on the maximum 1- and 5-day accumulated precipitation (i.e., Rx1day and Rx5day). The Rx1day and Rx5day in central China during TIF exceed the climatology of 1981–2010 by 51 and 130 mm, respectively, breaking historical records for the period of 1961–2021 (Figs. 3a,b). In eastern China, the Rx1day during TIF is slightly higher than the climatology by only 5 mm, while Rx5day is 54 mm, i.e., the fourth-highest event in the past 60 years (Figs. 3c,d).

Overall, the HPE in central China was extremely strong in terms of local precipitation. This event occurred ~2200 km poleward of the location of TIF, while the accumulated precipitation amount far exceeded 100 mm within 24 h. According to Cote (2007) and Galarneau et al. (2010), PREs occur over continental areas > 1000 km poleward of TCs (i.e., existing a clear separation between the two kinds of systems) and are associated with precipitation amounts exceeding 100 mm within 24 h. The distance and the accumulated precipitation amount (Fig. 2) suggest that the HPE in central China was a typical PRE indirectly triggered by TIF. However, the extremity of the HPE in eastern China is reflected in the accumulated total precipitation (Fig. 2a) rather than the daily precipitation peak, and is connected with the record-breaking duration of TIF's movement over eastern China and the neighboring seas. In a following study, we focus on analyzing how TIF triggered the PRE in central China and the circulation mechanisms of TIF's long-term movement over eastern China and the neighboring seas.

b. Synoptic patterns of TIF distantly triggering PRE in central China

1) MOISTURE CONFIGURATIONS

In this section, we explore how TIF remotely triggered the indirect HPE in central China from the perspective of PRE.

Brought to you by UNIVERSITY OF OXFORD-RADCLIFFE | Unauthenticated | Downloaded 09/18/23 11:06 AM UTC

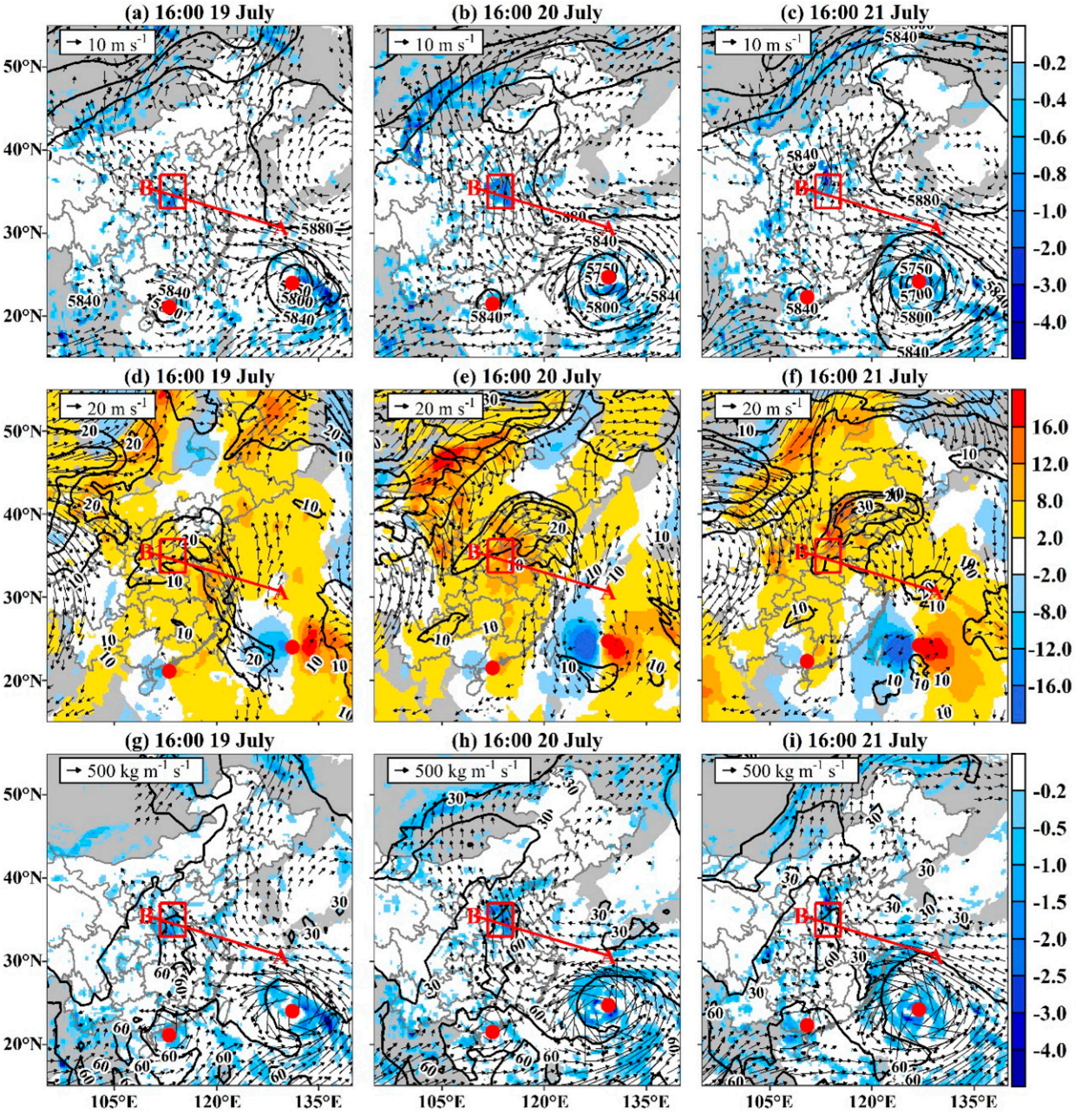

FIG. 4. Synoptic circulation of TIF indirectly triggering a predecessor rain event (PRE) in central China during 19–21 Jul 2021. (a)–(c) The 500-hPa geopotential height (black contour lines; unit: gpm), 500-hPa vertical velocity (blue shading; unit: Pa s^{-1}), and 700-hPa wind field (black arrows); (d)–(f) 200-hPa zonal wind (black contour lines; unit: m s^{-1}), 200-hPa wind field (black arrows), and 700-hPa meridional wind (colored shadows; unit: m s^{-1}); and (g)–(i) precipitable water (black contour lines; unit: mm), integrated water vapor transport (black arrows), and divergence of the integrated water vapor transport (blue shading; unit: 4 kg m^{-2} s^{-1}). The timing of the HPE peak in central China occurred at 1600 UTC 20 Jul (see Fig. 2b); therefore, we show the synoptic circulation at this time, 24 h earlier (i.e., 1600 UTC 19 Jul), and 24 h after (i.e., 1600 UTC 21 Jul). The line A–B in each panel denotes the main channel conveying abundant moisture. Two red dots represent the location of TIF (in the WNP) and Cempaka (in the South China Sea).

The PRE peak timing occurred at 1600 UTC 20 July; thus, we show circulation patterns at this time and in the prior and posterior 24 h (Figs. 4 and 5). At 1600 UTC 19 July, the western Pacific subtropical high (WPSH) was located over the Sea of Japan (Fig. 4a). The strong pressure gradient between the WPSH and TIF strengthened the southeasterly flow in the south of the WPSH, and steered TIF, conveying abundant tropical moisture from the western Pacific northwestward (Fig. 4g).

Brought to you by UNIVERSITY OF OXFORD-RADCLIFFE | Unauthenticated | Downloaded 09/18/23 11:06 AM UTC

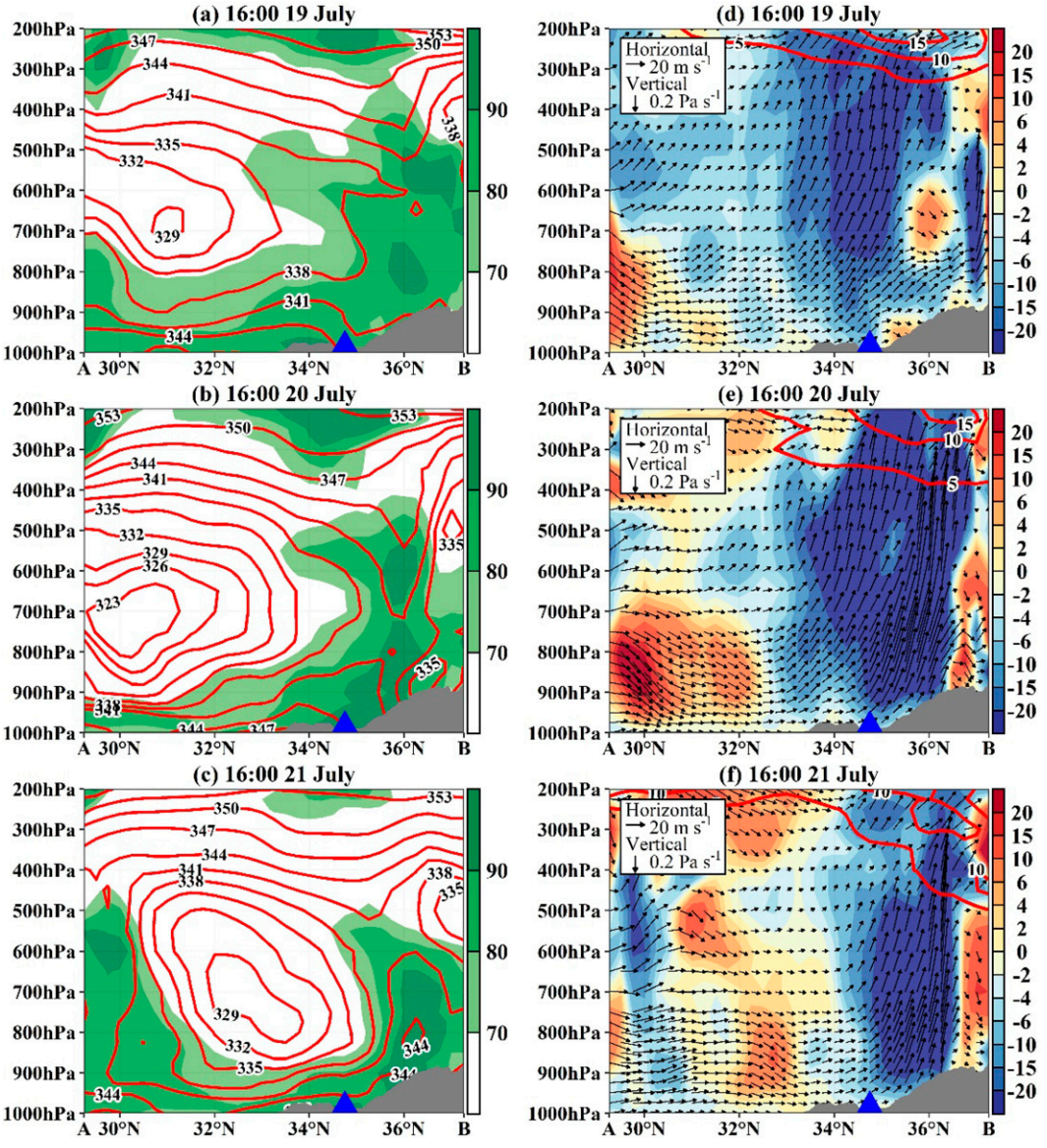

FIG. 5. As in Fig. 4, but for (a)–(c) vertical cross sections (along line A–B in Fig. 4) of relative humidity (shaded; unit: %) and equivalent potential temperature (red contours; unit: K); and (d)–(f) vertical velocity (shaded; unit: 10^{-2} Pa s^{-1}), zonal wind (red contours; unit: m s^{-1}), and flow (horizontal flow and vertical flow). The gray areas are terrain, and the blue triangle represents central China. The cross-sectional plots are along the line A–B (see Fig. S3), which passes through the Zhengzhou station, which experienced the record-breaking hourly precipitation (201.9 mm) and 24-h precipitation (552.5 mm) during TIF (F. Li et al. 2022). This line was expanded to a parallelogram region (the green polygon). We computed averaged variables in Fig. 5 over this region along latitude.

Correspondingly, high precipitable water with a maximum greater than 60 mm occurred in the surroundings of TIF (Fig. 4g). Abundant moisture might trigger thickening of the saturated moist layer, which is favorable for the occurrence of the PRE over central China.

Accompanying TIF's movement to China's mainland at 1600 UTC 20 July, the WPSH expanded farther westward and strengthened the southeasterly flow (Fig. 4b). The strengthened southeasterly flow brought abundant precipitable water, and the convergence of integrated water vapor flux spread northwestward from TIF's vicinity to central China (Fig. 4h). Similar results were reported by Nie and Sun (2022) who found that 30% and 38.1% of moisture was transported from the western North Pacific and southern China to central China. The southeasterly flow is a key factor for transporting abundant moisture from TIF's vicinity to central China. Zhao et al. (2022) found that the strong channel for conveying water vapor triggered by TIF and the WPSH played an essential role in the HPE in central China.

Brought to you by UNIVERSITY OF OXFORD-RADCLIFFE | Unauthenticated | Downloaded 09/18/23 11:06 AM UTC

The southwesterly flow also transported moisture from the vicinity of Typhoon Cempaka to central China; however, Typhoon Cempaka played a minor role in the occurrence of the PRE (Nie and Sun 2022; Yin et al. 2022).

2) LIFTING AND FRONTOGENESIS

An assessment of the main channel conveying abundant moisture during TIF (i.e., A–B line segment in Fig. 4 and Fig. S3) indicates that upward motion dominated in the south of central China and the periphery of the WPSH at 1600 UTC 19 July. This coincided quite well with mid- and low-level frontogenesis in the south of central China (Figs. 4a and 5a,d). Strong southeasterly flow appeared in the southern flank of the WPSH and impinged upon the mountains almost perpendicularly. This flow of abundant moisture triggered strong convergence, and thus forced ascent and frontogenesis on the windward slope (Figs. 5a,d). Strong ascent appeared from 1000 to 200 hPa on the windward slope over central China. Areas with high relative humidity (>80%) extended above 200 hPa. In addition, a slightly northerly downdraft appeared north of 36°N. The cold and dry flow moved southerly and collided with the southeasterly warm and moist air, resulting in the frontogenesis. To be specific, an anticyclone in the northern side of central China conveyed cold flow in the middle and upper atmosphere to the northwestern side of central China (Fig. S4a). This cold flow was dry and descended from the upper to the lower atmosphere, which is reflected by an obvious belt with low relative humidity and strong downward motion (see positive vertical velocity) in the northwest and north sides of central China in the upper atmosphere (Fig. S5a). This cold and dry flow in the middle and upper atmosphere in this heavy precipitation event in central China, has been also found in previous studies (Xue 2023; Yin et al. 2023). Furthermore, this dry and cold flow in the middle and upper atmosphere moved southward and collided with the southeasterly warm and moist flow, characterizing as a cyclone in the northwestern central China (Fig. S4a). The collision of the warm and cold flow contributed to the frontogenesis, and one of its manifestations was the denser isotherm (shown by equivalent potential temperature) in central China and its adjacent areas from 1600 UTC 19 July to 1600 UTC 20 July (Fig. S4).

At 1600 UTC 20 July, the southeasterly flow, ascent and frontogenesis were significantly intensified (Figs. 4b and 5b,e, Figs. S4b,e and S5b,e). This strengthened flow caused stronger convergence due to the orographic forcing effect, which intensified the frontogenesis. The stronger southeasterly wind conveyed abundant warm-moist air northward to central China. This increased the thermal gradient and intensified the frontogenesis in central China (Figs. 5b,e). The equivalent potential temperature reveals a ridge from 800 to 300 hPa in the north of central China, which intensified the instability of atmosphere, causing stronger deformation and frontogenesis in the central China. Accompanying the strengthening frontogenesis, the equivalent potential temperature lines became increasingly dense and uplifted northward over the central China (Figs. 5b,e). The constant motion from the lower to the upper troposphere over central China was conducive to lifting abundant moisture and weakening the instability of

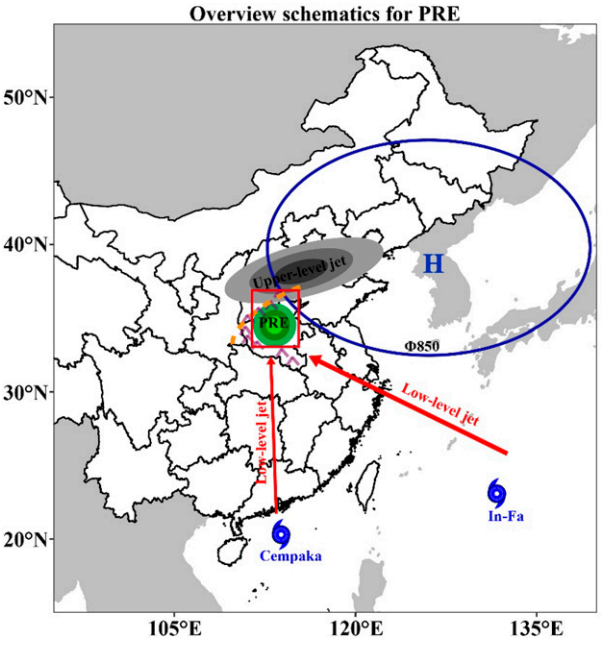

FIG. 6. Schematic illustrating the HPE remotely induced by TIF (i.e., PRE) in central China. The blue contour denotes the subtropical high (i.e., H). The dashed orange line is frontogenesis. The purple inverted-V symbols behind PRE represent mountains. The green shading marks the location of the PRE. The gray shading denotes the 200-hPa zonal wind with the central wind speed exceeding 30 m s^{-1}, indicating an upper-level jet. The red arrows mark 700-hPa meridional wind with the central wind speed exceeding 12 m s^{-1}, indicating a low-level jet.

atmosphere. At 1600 UTC 21 July, WPSH, the convergence of integrated water vapor flux, lifting motion, and frontogenesis all weakened in central China (Figs. 4c,i and 5c,f, Figs. S4c,f and S5c,f), resulting in the weakening of the PRE in central China.

An upper-level westerly jet (i.e., upper-level circulation) can be found in the north of central China (Figs. 4d–f). Before 1600 UTC 21 July, this jet gradually developed and contributed to the occurrence of the PRE. Abundant moisture was transported northward by TIF and Typhoon Cempaka, steered by the southwesterly flow and southeasterly flow (presented as two low-level jets; Luo and Du 2023), and forced to ascend along the frontogenesis in the equatorward entrance region of the upper-level westerly jet (Figs. 4d–f and 5). Conversely, heavy precipitation-producing systems (e.g., TIF and the PRE) with deep ascent and strong latent heat release drove the outflow divergently and adiabatically in the upper level, and thus intensified the upper-level westerly jet (Bosart et al. 2012; see Fig. S2). From 1600 UTC 19 July to 1600 UTC 20 July (Figs. 4d,e and Figs. S2a,b), an upper-level westerly jet developed in the north of central China and contributed to the occurrence of the PRE in central China. Meanwhile, there was a clear increased divergence (blue areas) above central China. At 1600 UTC 20 July, weaker potential vorticity and stronger irritational wind showed in the south and west of the upper-

Brought to you by UNIVERSITY OF OXFORD-RADCLIFFE | Unauthenticated | Downloaded 09/18/23 11:06 AM UTC

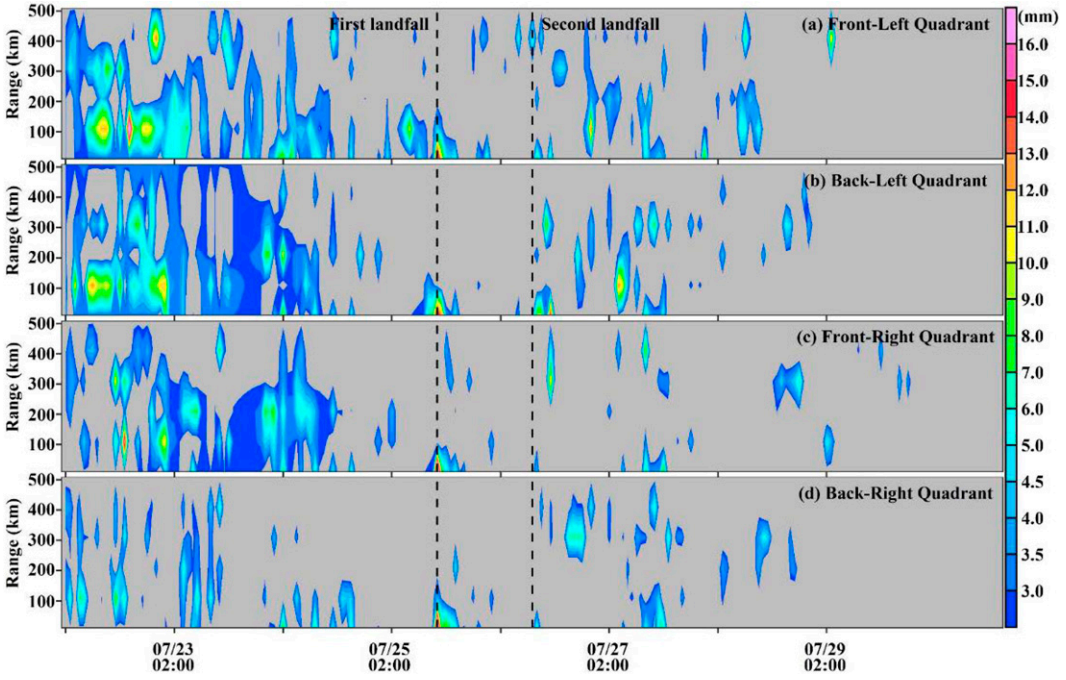

FIG. 7. Satellite-based hourly precipitation distribution (based on hourly global real-time satellite precipitation) as a function of distance to TIF's center. The precipitation under the direct effects of TIF is decomposed into four different quadrants (i.e., front-left, back-left, front-right, and back-right quadrants) according to the direction of TIF's propagation during 22–29 Jul 2021. The dashed vertical black lines indicate the time of the first and second landfalls.

level westerly jet compared with 1600 UTC 19 July, which reinforced the intensified westerly jet. Therefore, weaker potential vorticity, which was accompanied by diabatically driven outflow of the PRE and concentrated in the entrance of the upper-level westerly jet due to irrotational wind, might lead to large potential vorticity gradient and the intensification of the upper-level westerly jet. At 1600 UTC 21 July, this jet showed eastward displacement, accompanying the weakening PRE in central China (Fig. 4e).

Note that there were lower zonal wind values at 300 hPa and no zonal wind below ~400 hPa (Figs. 5b,d,e). We computed averaged zonal wind components over the A–B line and its extended region along latitude (see Fig. S3), which might offset the high zonal wind values. To better show the zonal wind distribution, we plotted the zonal wind and wind field at 300, 400, and 500 hPa (see Figs. S6 and S7). Taking 1600 UTC 20 July (Figs. S6a,e,h) as an example, the 300-hPa zonal wind value is greater in the northwestern part (i.e., >5 m s^{-1}), and smaller in the southeastern part. When we computed the mean zonal wind value along latitude, the high values in the northwestern part were offset by the lower values in the southeastern part. Meanwhile, Fig. S7 showed a stronger easterly in the southeastern part, which decreased the zonal wind values. Therefore, the zonal wind values at 300 hPa were relatively lower. When we shifted to 400-hPa and lower levels (Figs. S6 and S7e,h), the lower zonal wind value in the northeastern part and stronger easterly at most half of the eastern part further reduced the zonal wind component, which is why there were no zonal wind contours below ~400 hPa. Although some of our analyses (i.e., moisture transport, easterly flow and ascent) are similar to previous studies, no study has analyzed the frontogenesis and upper-level circulation in the indirect HPE in central China at present, to the best of our knowledge. Part of our results are consistent with previous studies, which adds further confidence in our analyses about frontogenesis and upper-level circulation in this study.

3) OVERVIEW SCHEMATICS OF TIF DISTANTLY TRIGGERING PRE IN CENTRAL CHINA

Figure 6 shows a summary schematic of TIF remotely triggering PRE in central China. In the southeast and south of central China, two strong flows (i.e., southeasterly and southwesterly flows), which present as low-level jets, moved northward along the strong channel between the WPSH and TIF and only Typhoon Cempaka, conveyed abundant tropical moisture from the vicinity of TIF and Typhoon Cempaka to central China, respectively. These flows with abundant moisture triggered strong convergence, forcing ascent due to the impacts of orographic forcing and frontogenesis on the windward slope, resulting in the occurrence of the PRE. Zhang et al. (2022) found that the similar strong easterly flow and upward motion anomaly that generated this PRE also led to another catastrophic HPE in August 1975 in central China. In this study, the PRE was located beneath the equatorward entrance of the upper-level westerly jet and interacted with this jet as well. The PRE associated with deep ascent and strong latent heat release

Brought to you by UNIVERSITY OF OXFORD-RADCLIFFE | Unauthenticated | Downloaded 09/18/23 11:06 AM UTC

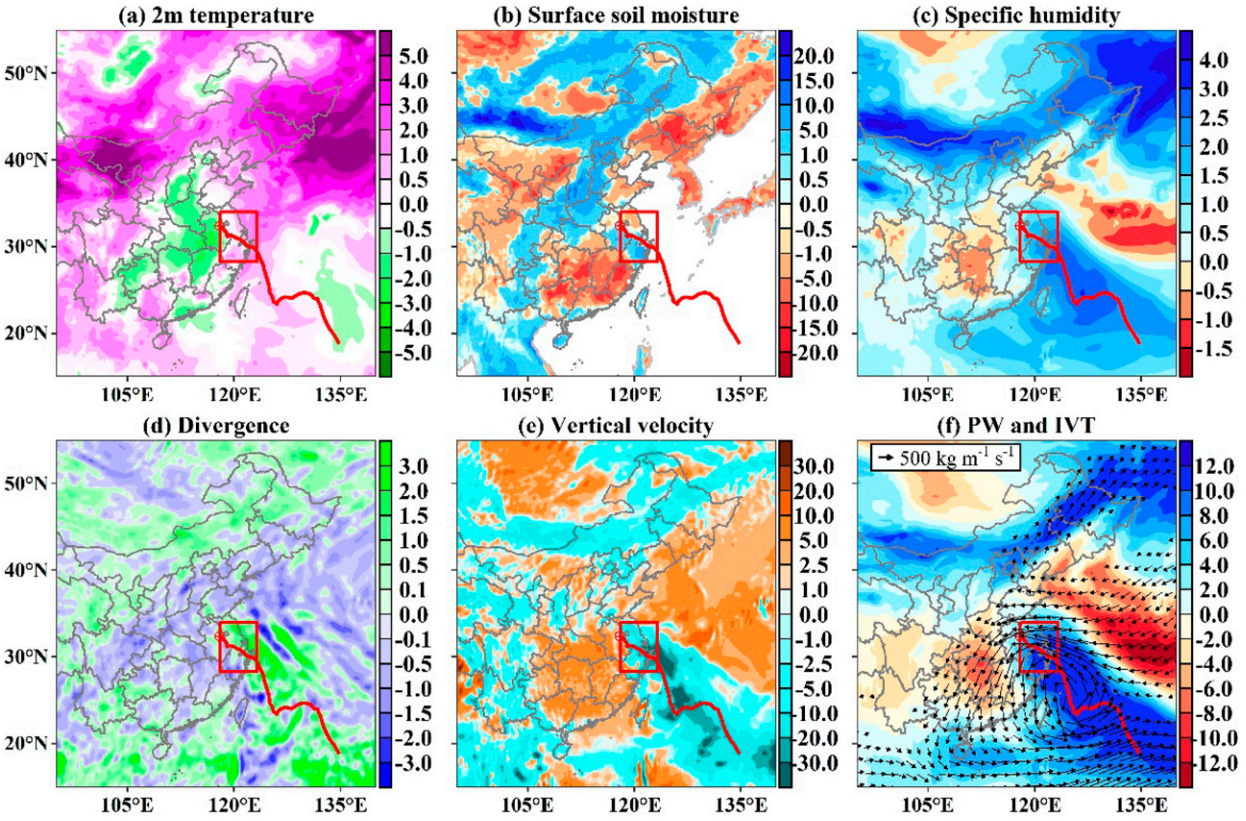

FIG. 8. Anomaly analysis of synoptic circulation for TIF during the HPE in eastern China during (a) 17–24 Jul and (b)–(f) 22–27 Jul relative to the summer (June–August) climatology of 1981–2010. The 2-m temperature and other variables during TIF are averaged based on 17–24 Jul and 22–27 Jul, respectively. Color shading in (a)–(f) represents 2-m temperature (unit: K), surface soil moisture (unit: 10^{-2} m^3 m^{-3}), 700–1000-hPa specific humidity (unit: 10^{-3} kg kg^{-1}), 200-hPa divergence (unit: 10^{-5} s^{-1}), 500-hPa vertical velocity (unit: 10^{-2} Pa s^{-1}), and precipitable water (shaded, unit: mm), respectively. In (f), vectors represent integrated water vapor transport.

was beneficial for driving divergent and adiabatic outflow in the upper level, and then intensified the upper-level westerly jet.

c. *Synoptic patterns of TIF directly producing the HPE in eastern China*

1) EVOLUTION OF PRECIPITATION DISTRIBUTION OVER LAND

In comparison with the remote PRE in central China, the HPE in eastern China was directly linked with the direct effects of TIF. Therefore, we first describe the precipitation distribution as a function of distance to TIF's center. Instead of considering the usual geographic directions (i.e., east, west, south, and north), we use the Lagrangian approach (Villarini et al. 2011) to investigate the radial precipitation distribution from four different quadrants (i.e., the front-left, back-left, front-right, and back-right quadrants) with respect to the propagation direction of TIF. This method enables a detailed analysis of the spatial–temporal evolution of precipitation triggered by landfalling TIF (Villarini et al. 2011).

The left quadrants (i.e., the front-left and the back-left quadrants) of TIF experienced more precipitation (Figs. 7a,b). Before landfall, the maximum precipitation tended to be concentrated within 50–200 km from the center of TIF. At the time of the first landfall, the precipitation maximum was concentrated within 50 km of TIF's center, suggesting a trend of the collapse of TIF's eye (Villarini et al. 2011). As TIF progressed farther inland, the maximum precipitation tended to decrease and move away from TIF's center, dissipating after 28/29 July. As mentioned above, the direct HPE in eastern China was mainly concentrated within 200 km from the center of TIF and even in the vicinity of TIF's eye. Therefore, the HPE in eastern China can mainly be explained by TIF's position and duration over land. As shown in Fig. 3, it was the accumulated precipitation (i.e., Rx5day), rather than the short-term precipitation (Rx1day), which was extreme. For instance, some stations (e.g., station Siyang and Jiangdu; see Fig. 12 for the locations of the two stations) in eastern China witnessed record-breaking accumulated precipitation values (322.3 and 319.0 mm, respectively), due to the long duration and slow movement of TIF in eastern China.

2) LONG DURATION OF TIF

The average translation speed of TIF during its lifetime was 10.6 km h^{-1}, which is approximately 51% lower than that of all typhoons over the WNP during 1961–2021 based on the

Brought to you by UNIVERSITY OF OXFORD-RADCLIFFE | Unauthenticated | Downloaded 09/18/23 11:06 AM UTC

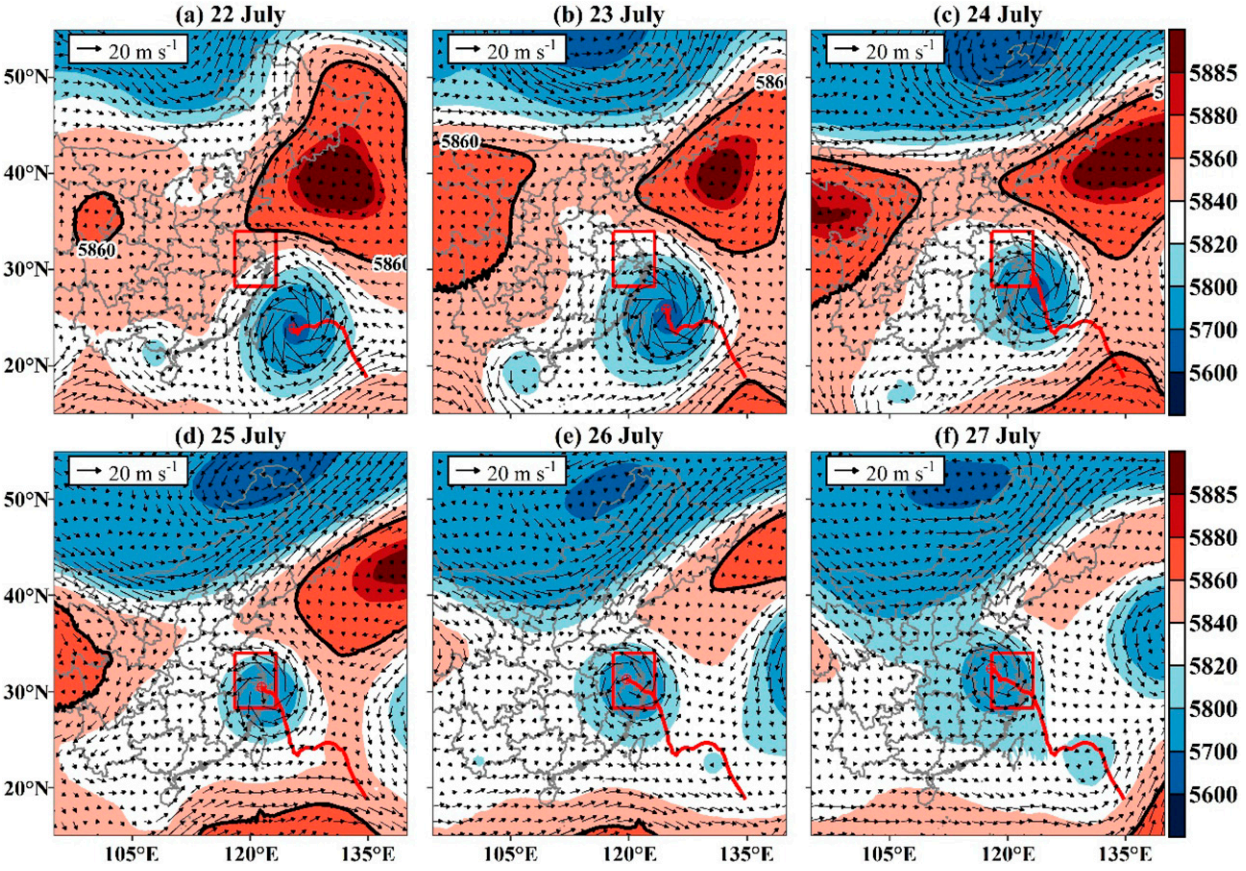

FIG. 9. Synoptic circulations for TIF during the direct HPE in eastern China during 22–27 Jul. The shaded areas represent 500-hPa geopotential height (unit: gpm). The vectors indicate 500-hPa steering flow. The black lines represent the 5860-gpm line that is used to identify the location of the subtropical high. The red lines represent TIF tracks at the given time.

IBTrACS TC best track dataset. The total overland duration of TIF (>90 h) was 3.5 times longer than the average overland duration (20 h) of all landfalling typhoons over the WNP. However, the total translation distance of TIF is 3491 km, which is 61% of the average translation distance (5760 km) of all typhoons over the WNP. The unusually low translation speed, long duration, and short translation distance indicate that TIF stalled and meandered over eastern China, which explains the anomalous persistent heavy precipitation in this region.

The World Meteorological Organization defines the 30-yr normal period of 1981–2010 as a climatological baseline period which is popular among present studies for anomaly analysis of a group of events or a single extreme event (Hoerling et al. 2013; Blunden and Arndt 2017; Fazel-Rastgar 2020; Li et al. 2021; Overland and Wang 2021; Hermanson et al. 2022). Here, for the first time, to the best of our knowledge, we discuss the possible reasons for the long duration of TIF by using anomaly analysis. Before the landfall of TIF (17–24 July), 2-m temperature showed positive anomalies in eastern China and the neighboring seas (Figs. 8a,b), which was conducive to the intensification of TIF before landfall and its maintenance on land. After TIF's landfall, the enhanced surface roughness and the decrease in high heat and ocean-derived moisture flux led to the weakening intensity of TIF. However, these energy losses could be compensated by the enhancement of surface heat flux (Shen et al. 2002; Emanuel et al. 2008; Andersen and Shepherd 2014; Hlywiak and Nolan 2021). The warmer 2-m temperature was conducive to the enhancement of sensible heat and the mitigation of the cooling rate of the warm core after TIF made landfall (Fig. 8a). The wetter surface soil moisture and the low-level (1000–700 hPa) specific humidity were conducive to the longer-lasting release of latent heat, resulting in a slower rate of decay of and increasing the duration of TIF over land (Figs. 8b,c).

In addition to the favorable thermodynamic conditions mentioned above, dynamic factors (such as positive divergence anomalies in the upper troposphere and ascending motion anomalies in the middle troposphere over eastern China) also contributed to TIF's maintenance in eastern China (Figs. 8d,e). Abundant atmospheric moisture also played a key role in TIF's maintenance in eastern China (Fig. 8f). Eastern China and the neighboring seas experienced positive precipitable water anomalies and a cyclonic convergence of the integrated water vapor flux. The increased humidity in a TC's periphery is conducive to an intensification of the TC

Brought to you by UNIVERSITY OF OXFORD-RADCLIFFE | Unauthenticated | Downloaded 09/18/23 11:06 AM UTC

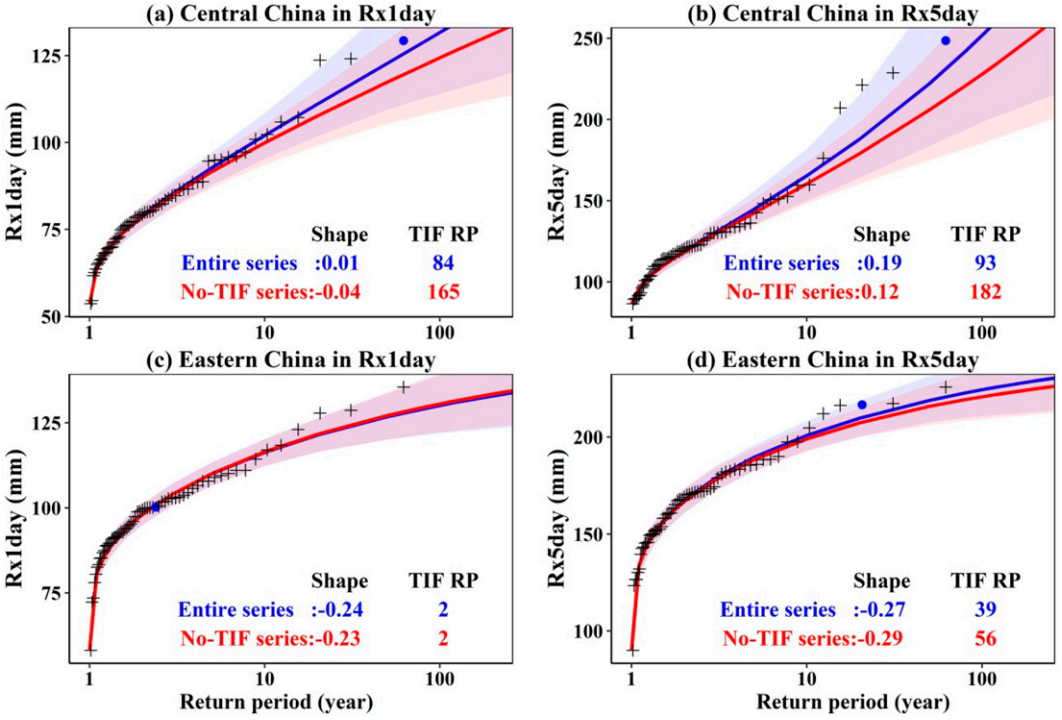

FIG. 10. Return periods based on heavy precipitation series (i.e., Rx1day and Rx5day; based on observed station-based hourly precipitation) in central China and eastern China during 1961–2021. Blue (red) curves indicate the return period based on the entire series (or no-TIF series, i.e., removing the TIF-induced HPE). "Shape" and "TIF RP" values in each panel indicate the shape parameters of the GEV distribution and the return periods of the HPE triggered by TIF. Black crosses are the HPEs during 1961–2020, and blue dots are the HPEs induced by TIF in 2021.

and an increased probability of precipitation (Kimball 2006; Jiang et al. 2008; Hill and Lackmann 2009).

3) SLOW MOVEMENT OF TIF

The pressure field and steering flow anomalies played a key role in the slowdown of TIF (Fig. 9). On 22 July, a saddle-shaped field was formed by the continental high and the subtropical high in the north of eastern China, impeding TIF's movement northward. Meanwhile, the weakened steering flow in the periphery of TIF was too feeble to guide TIF northward (Figs. 9a–d). Yang et al. (2022) have indicated that the speed of steering flow was lower than that of TIF's movement due to large-scale circulation conditions. It was challenging for the weak steering flow to drive the forward movement of TIF. After 27 July, an eastward movement and a southward extension of the westerly trough cut off the saddle-shaped field, and this also was accompanied by a weakened eastward WPSH (Figs. 9e,f). These results are consistent with Zhang (2021), who found that TIF merged into the westerly trough; the steering flow in front of the westerly trough became strengthened, and thus TIF's northward movement accelerated.

The impact of climate change on TCs in the WNP has engendered considerable interest. According to observations since 1961, anthropogenic climate change has increased the frequency of TC-induced HPEs (Utsumi and Kim 2022). Furthermore, Lai et al. (2020) detected an anthropogenic forcing component to the observed decrease in TC translation speeds over the WNP. These findings imply that the TIF-induced HPE and slow movement of TIF in eastern China and adjacent areas might be related to anthropogenic climate change.

d. *Impact of TIF on return period estimations of local HPEs*

The HPEs that were distantly triggered by TIF in central China or directly produced by TIF in eastern China were particularly extreme, causing huge economic losses, infrastructure damages and casualties. To prevent or reduce these damages, hydraulic engineering infrastructure (such as open channels and pipes) is designed based on return periods. However, the magnitude of the indirect and direct HPEs triggered by TIF in central and eastern China was so extreme that they likely altered the return period estimates of local HPEs. Major changes in the return periods of HPEs can significantly affect security risk evaluations and the flood control ability of local hydraulic engineering infrastructure. Here, a mixed population approach of the area-averaged Rx1day and Rx5day time series generated by different mechanisms was used. As shown in Fig. 10, the HPEs triggered by TIF led to an increase in the shape parameters of the GEV distribution in both central and eastern China, resulting in heavier upper tails of the local heavy precipitation frequency curves (apart from Rx1day in eastern China). For instance, in central China, the shape parameters of the entire series of Rx1day and Rx5day (0.01 and

Brought to you by UNIVERSITY OF OXFORD-RADCLIFFE | Unauthenticated | Downloaded 09/18/23 11:06 AM UTC

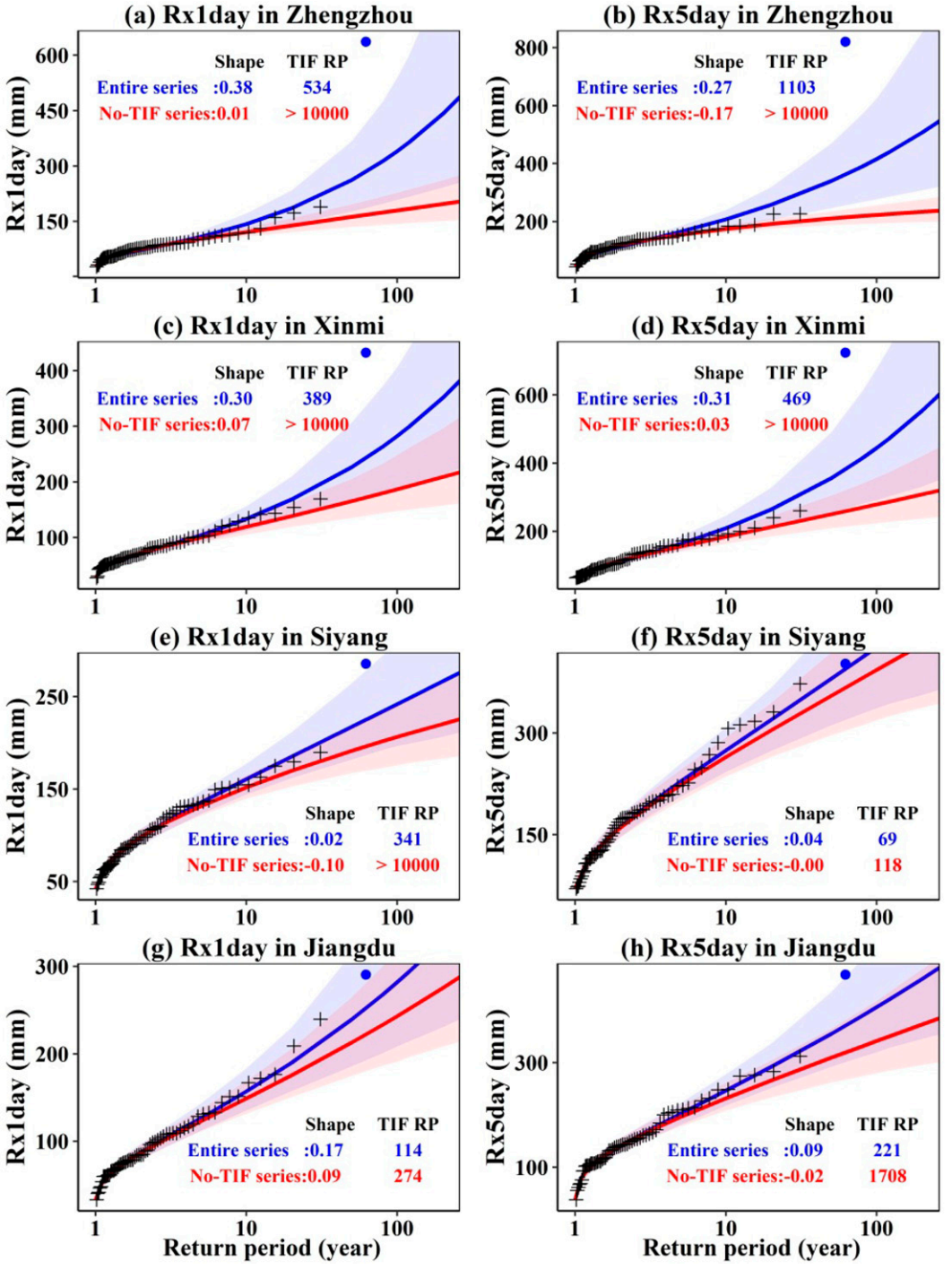

FIG. 11. As in Fig. 10, but for typical stations in central China (Zhengzhou and Xinmi) and eastern China (Siyang and Jiangdu). Please see the locations of the four stations in Fig. 12.

0.19) were larger than those (−0.04 and 0.12) of the no-TIF series (i.e., with the TIF-induced HPE removed). Dare et al. (2012) also found that TCs tend to increase the shape parameter of the heavy precipitation frequency curve. Gu et al. (2017) found that TCs tend to increase the shape parameter and the thick upper tails of heavy precipitation frequency curves.

In addition, the TIF-induced HPE might change the GEV distribution and shape parameter, which further influenced the upper tail of heavy precipitation frequency curve and changed return period estimations. In central China, the return periods of the Rx1day and Rx5day that occurred during TIF are estimated as 84 and 93 years based on the entire heavy precipitation

Brought to you by UNIVERSITY OF OXFORD-RADCLIFFE | Unauthenticated | Downloaded 09/18/23 11:06 AM UTC

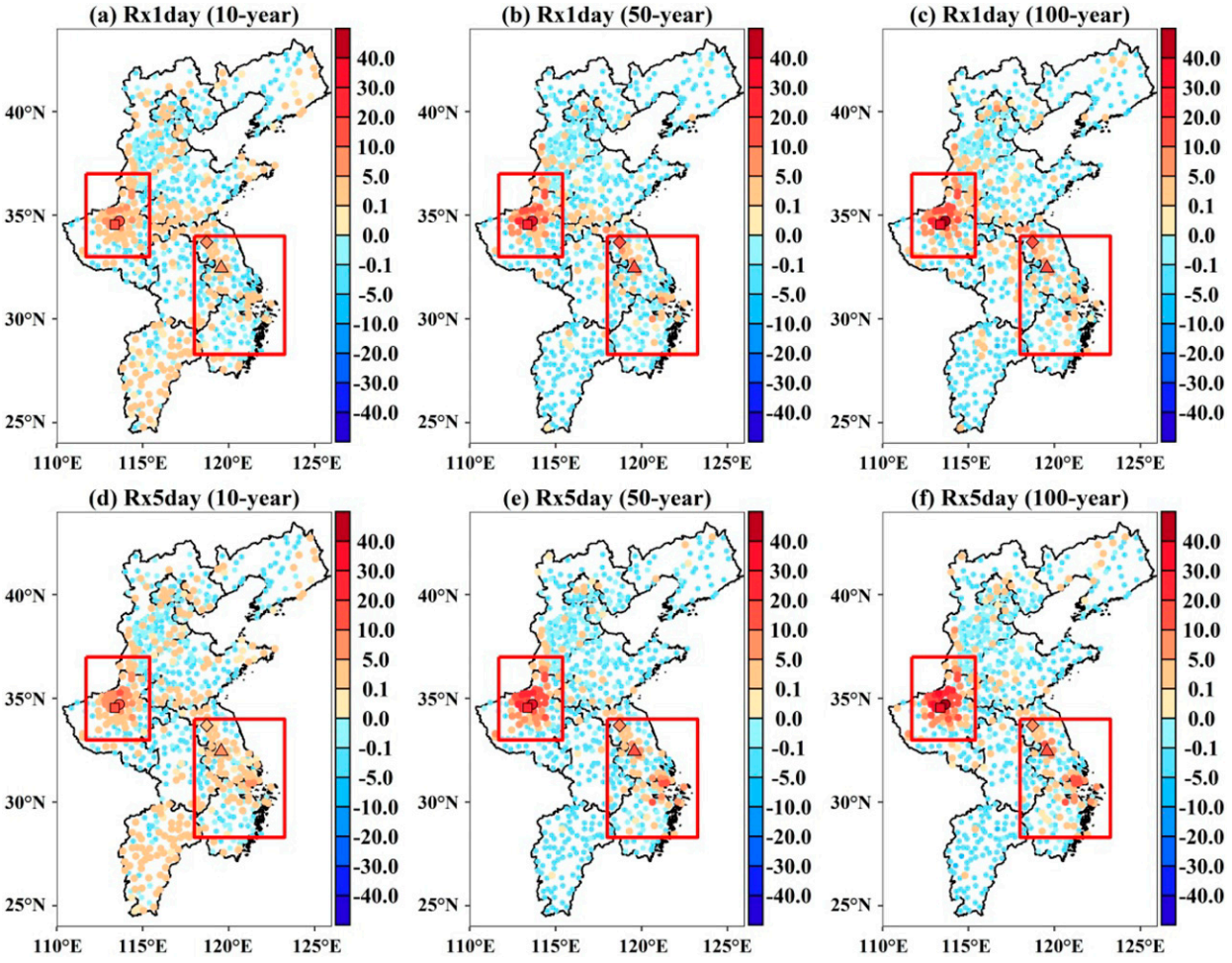

FIG. 12. Relative percent differences (RPDs; unit: %) between the GEV estimates from the precipitation series (i.e., Rx1day and Rx5day; based on observed station-based hourly precipitation) with the TIF-induced HPE included and removed. The RPDs are estimated for the (a),(d) 10-; (b),(e) 50-; and (c),(f) 100-yr return periods. The dot, square, diamond, and triangle in each panel represent stations Zhengzhou, Xinmi, Siyang, and Jiangdu, respectively.

series, respectively; however, if one excludes the TIF-induced events, the same return periods increase to 165 and 182 years (i.e., lower chance of occurrence; Figs. 10a,b). Similar results are found in eastern China, especially for the Rx5day (Fig. 10d). For the stations where the TIF-induced precipitation extremes were record-breaking, the above results are even more obvious (Fig. 11). Taking station Zhengzhou as an example, the Rx1day induced by TIF is 636.7 mm, which is 447.3 mm larger than the second largest value during 1961–2021. The return period of the Rx1day induced by TIF in this station is estimated as 534 years using the entire series, but exceeds 10 000 years when excluding the TIF-induced event (Fig. 11a). It is important to note that the uncertainty of the upper tail of heavy precipitation frequency curves is always considerable and the inclusion of record-breaking events may contribute to even greater uncertainty (Fig. 11). Unprecedented HPEs (i.e., TIF-induced HPEs) can change the shape parameter and GEV distribution, such that the return period based on the original GEV distribution would be overestimated and thus lead to an underestimation of the risk of heavy precipitation. Therefore, the hydraulic engineering infrastructure designed using the original distribution would fail to meet the required design standard (i.e., return period), especially in inland areas (e.g., central China).

TIF led to a decrease in the estimated return period of the HPEs, which is also reflected in the relative percent differences (i.e., RPD) between the estimated precipitation magnitudes from the heavy precipitation series (i.e., Rx1day and Rx5day) computed with the TIF-induced HPE included and removed (Fig. 12). Both the Rx1day and Rx5day in central China exhibit positive RPD values for the 10-, 50-, and 100-yr return periods. The positive RPD is especially visible for the 100-yr return period, with RPD values above 40%. This indicates that the GEV estimates from the entire precipitation series (i.e., including the HPEs triggered by TIF) are higher than those estimated from the no-TIF series (i.e., removing the HPEs triggered by TIF). In eastern China, however, positive RPD values are found in a much smaller number of stations, and are more visible for the Rx5day.

Brought to you by UNIVERSITY OF OXFORD-RADCLIFFE | Unauthenticated | Downloaded 09/18/23 11:06 AM UTC

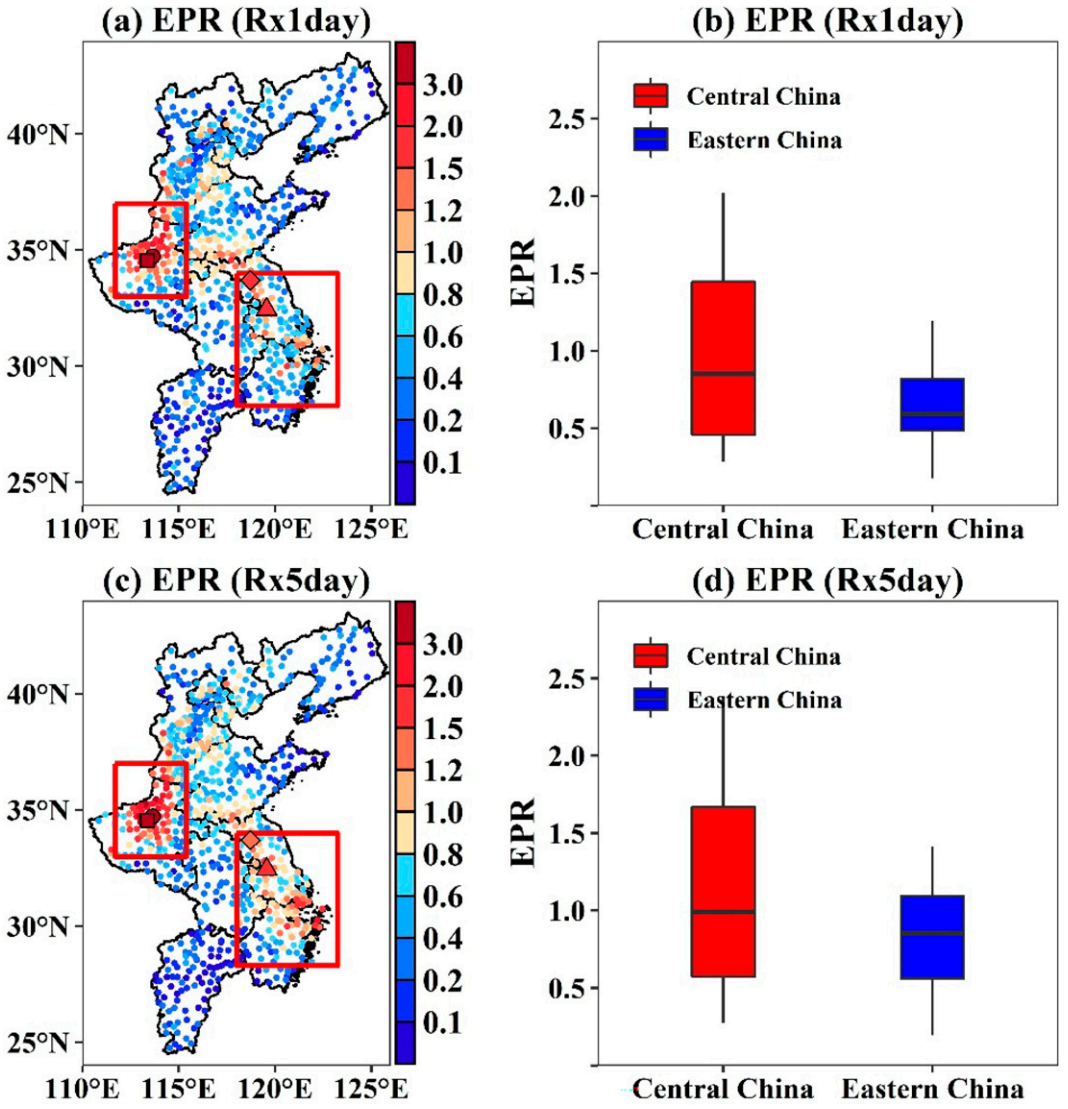

FIG. 13. Extreme precipitation ratio (EPR) (a),(c) maps and (b),(d) boxplots for the Rx1day and Rx5day based on observed station-based hourly precipitation during the period of TIF in central China and eastern China, respectively. The dot, square, diamond, and triangle in each panel represent stations Zhengzhou, Xinmi, Siyang, and Jiangdu, respectively.

The extreme precipitation ratio (EPR; HPEs normalized by their 10-yr precipitation peak) is employed (see Methods) to estimate the relative magnitude of the TIF-induced HPEs at a local scale and compare the relative influence of the TIF-induced HPEs between central China and eastern China (Fig. 13). Central China is dominated by EPR values above 1 (even 3 in several stations) for both Rx1day and Rx5day, suggesting that the TIF-induced HPE was much higher than the local 10-yr heavy precipitation. However, ERP values above 1 only occur in several stations in eastern China for both the Rx1day and the Rx5day. Boxplots in Figs. 13b and 13d also show that EPR values for the Rx1day and Rx5day in central China are notably higher than those in eastern China, suggesting a larger local relative influence of the TIF-induced heavy precipitation in central China.

Usually, TC-triggered averaged and extreme precipitation magnitudes gradually decrease from the coastal areas to the inland areas (Zhang et al. 2011; Khouakhi et al. 2017). TCs also tend to cause more catastrophic losses in coastal areas compared with inland areas, therefore there already exists a range of infrastructure for mitigating TC-induced HPE disasters in coastal areas. However, our results indicate that TIF had a higher impact on the return period estimates of the HPE in the inland areas (i.e., central China) than in the coastal areas (i.e., eastern China), markedly reducing return period estimates of HPEs in the inland areas. Similarly, Villarini et al. (2014) also found that hurricanes are responsible for major flooding in inland areas of the United States. TC-induced HPEs (especially PREs) pose a serious challenge for the safety

Brought to you by UNIVERSITY OF OXFORD-RADCLIFFE | Unauthenticated | Downloaded 09/18/23 11:06 AM UTC

of flood control projects in inland areas. These findings indicate that more attention should be paid to such HPEs when estimating the design values of hydraulic engineering infrastructure, especially in inland areas.

4. Summary

In this study we focused on the HPEs indirectly and directly triggered by TIF in central and eastern China, which caused catastrophic losses of life and property. We evaluated the spatiotemporal evolution of the two HPEs and examined the synoptic patterns during TIF for both. We revealed the moisture configurations, lifting and frontogenesis and upper-level jet during the HPE indirectly triggered by TIF, producing the first such analysis, to the best of our knowledge. For the direct HPE in eastern China, we uncovered the evolution of the precipitation distribution as a function of distance (≤500 km) to TIF's center. Additionally, we conducted an anomaly analysis to explain the long duration and slow movement of TIF. Finally, we explored the impact of TIF on return period estimations by using the GEV distribution. Our results showed that TIF triggered the HPE remotely in central China during 19–21 July 2021, and this HPE was a typical PRE. Two low-level jets (i.e., southeasterly and southwesterly flow) conveyed abundant moisture from the vicinity of TIF and Typhoon Cempaka to central China, respectively. Due to the impacts of orographic forcing, these flows of abundant moisture triggered strong convergence and forced ascent and frontogenesis on the windward slope, thereby generating the PRE in central China. The PRE was located beneath the equatorward entrance of the upper-level westerly jet. Conversely, the deep ascent and strong latent heat release was beneficial for driving divergent and adiabatic outflow in the upper level, which then intensified the strength of the upper-level westerly jet.

The HPE in eastern China was mainly located in areas situated less than 200 km from TIF's center, and along the front-left and back-left quadrants of TIF's propagation trajectory. The anomalous HPE is reflected in the accumulated precipitation totals during TIF associated with the long duration and slow movement of TIF. On the one hand, anomaly analysis showed that the thermodynamic (warmer 2-m temperature, wetter soil surface moisture, higher low-level specific humidity), and dynamic (stronger midlevel vertical velocity and upper-level divergence) conditions sustained TIF's intensity. Additionally, the availability of abundant precipitable water and the cyclonic convergence of the integrated water vapor not only slowed TIF's decay and but also strengthened the HPE in eastern China. On the other hand, a saddle-shaped pressure field was formed from the continental high and the WPSH, and weak steering flow occurred in the south of the WPSH, which hindered TIF's movement northward.

Both the HPEs distantly and directly induced by TIF were exceptionally extreme, resulting in a notable alteration in the shape of the heavy precipitation frequency curves, with an increased shape parameter and heavier upper tails of the frequency distribution. The return period estimated using the original GEV distribution (prior to the inclusion of the TIF-induced HPEs) would thus be overestimated, i.e., underestimating the risk of heavy precipitation. The decrease in return period estimates after the inclusion of the TIF-induced HPEs is also reflected in positive RPD between the estimated precipitation magnitudes obtained from the precipitation series (i.e., Rx1day and Rx5day) computed with and without the TIF-induced HPE. The positive RPD reveals that the TIF-induced HPE is more extreme compared with the HPEs induced by other mechanisms in central China. The local relative magnitudes of the TIF-induced HPEs were notably larger in central China, compared with eastern China. Our results suggest that disaster management agencies should enhance the prevention and early warning of anomalous HPEs distantly triggered by TCs, and more attention should be paid to such HPEs when estimating the design values of hydraulic infrastructure in inland areas.

Acknowledgments. This study is supported by the following projects: the National Natural Science Foundation of China (Grants U1911205 and 41901041), the Pre-research Project of SongShan Laboratory (YYYY062022001), the Guiding project of Scientific Research Plan of Education Department of Hubei Province (Grant B2022265), and the open funding from State Key Laboratory of Water Resources and Hydropower Engineering Science (Wuhan University) (Grant 2021SWG01). Xihui Gu is supported by the China Scholarship Council. Louise Slater is supported by UKRI (MR/V022008/1) and NERC (NE/S015728/1). The authors declare that they have no known competing financial interests or personal relationships that could have influenced the work reported in this paper.

Data availability statement. The observed station-based and gridded precipitation data were obtained from the China Meteorological Data Service Center (http://www.nmic.cn/en). Hourly global real-time satellite precipitation data are available at https://chrsdata.eng.uci.edu/. The tropical cyclone best track dataset was obtained from the International Best Track Archive for Climate Stewardship (https://www.ncdc.noaa.gov/ibtracs/). The ERA5 dataset is available at https://www.ecmwf.int/en/forecasts/datasets/reanalysis-datasets/era5.

REFERENCES

Aiyelokun, O., Q. B. Pham, O. Aiyelokun, A. Malik, S. Adarsh, B. Mohammadi, N. T. T. Linh, and M. Zakwan, 2021: Credibility of design rainfall estimates for drainage infrastructures: Extent of disregard in Nigeria and proposed framework for practice. *Nat. Hazards*, **109**, 1557–1588, https://doi.org/10.1007/s11069-021-04889-1.

Andersen, T. K., and J. M. Shepherd, 2014: A global spatiotemporal analysis of inland tropical cyclone maintenance or intensification. *Int. J. Climatol.*, **34**, 391–402, https://doi.org/10.1002/joc.3693.

Baek, E.-H., J.-H. Kim, J.-S. Kug, and G.-H. Lim, 2015: Midtropospheric frontogenesis associated with antecedent indirect precipitation ahead of tropical cyclones over the Korean Peninsula. *Tellus*, **67A**, 27476, https://doi.org/10.3402/tellusa.v67.27476.

Barth, N. A., G. Villarini, M. A. Nayak, and K. White, 2017: Mixed populations and annual flood frequency estimates in the

Brought to you by UNIVERSITY OF OXFORD-RADCLIFFE | Unauthenticated | Downloaded 09/18/23 11:06 AM UTC

western United States: The role of atmospheric rivers. *Water Resour. Res.*, **53**, 257–269, https://doi.org/10.1002/2016WR019064.

Ben Alaya, M. A., F. Zwiers, and X. Zhang, 2020: An evaluation of block-maximum-based estimation of very long return period precipitation extremes with a large ensemble climate simulation. *J. Climate*, **33**, 6957–6970, https://doi.org/10.1175/JCLI-D-19-0011.1.

Blunden, J., and D. S. Arndt, 2017: State of the climate in 2016. *Bull. Amer. Meteor. Soc.*, **98** (8), Si–S280, https://doi.org/10.1175/2017BAMSStateoftheClimate.1.

Bosart, L. F., J. M. Cordeira, T. J. Galarneau Jr., B. J. Moore, and H. M. Archambault, 2012: An analysis of multiple predecessor rain events ahead of Tropical Cyclones Ike and Lowell: 10–15 September 2008. *Mon. Wea. Rev.*, **140**, 1081–1107, https://doi.org/10.1175/MWR-D-11-00163.1.

Cavanaugh, N. R., A. Gershunov, A. K. Panorska, and T. J. Kozubowski, 2015: The probability distribution of intense daily precipitation. *Geophys. Res. Lett.*, **42**, 1560–1567, https://doi.org/10.1002/2015GL063238.

Chan, F. K. S., and Coauthors, 2022: Lessons learnt from Typhoons Fitow and In-Fa: Implications for improving urban flood resilience in Asian coastal cities. *Nat. Hazards*, **110**, 2397–2404, https://doi.org/10.1007/s11069-021-05030-y.

Cheng, J. B., Y. Zhao, R. Zhi, and G. Feng, 2022: Analysis of the July 2021 extreme precipitation in Henan using the novel moisture budget equation. *Theor. Appl. Climatol.*, **149**, 15–24, https://doi.org/10.1007/s00704-022-04022-7.

Cooley, D., 2012: Return periods and return levels under climate change. *Extremes in a Changing Climate: Detection, Analysis and Uncertainty*, A. AghaKouchak et al., Eds., Springer, 97–114.

Cote, M. R., 2007: Predecessor rain events in advance of tropical cyclones. M.S. thesis, Dept. of Atmospheric and Environmental Sciences, University at Albany, State University of New York, 200 pp.

Czajkowski, J., G. Villarini, E. Michel-Kerjan, and J. A. Smith, 2013: Determining tropical cyclone inland flooding loss on a large scale through a new flood peak ratio-based methodology. *Environ. Res. Lett.*, **8**, 044056, https://doi.org/10.1088/1748-9326/8/4/044056.

Dare, R. A., N. E. Davidson, and J. L. McBride, 2012: Tropical cyclone contribution to rainfall over Australia. *Mon. Wea. Rev.*, **140**, 3606–3619, https://doi.org/10.1175/MWR-D-11-00340.1.

de Lange, W. P., and J. G. Gibb, 2000: Is the Annual Exceedence Probability (AEP) an appropriate tool for quantifying extreme coastal water level hazard? *Int. Coastal Symp. 2000*, Rotorua, New Zealand, Per Bruun, 1–122.

Emanuel, K., J. Callaghan, and P. Otto, 2008: A hypothesis for the redevelopment of warm-core cyclones over northern Australia. *Mon. Wea. Rev.*, **136**, 3863–3872, https://doi.org/10.1175/2008MWR2409.1.

Fazel-Rastgar, F., 2020: Extreme weather events related to climate change: Widespread flooding in Iran, March–April 2019. *SN Appl. Sci.*, **2**, 2166, https://doi.org/10.1007/s42452-020-03964-9.

Fowler, H. J., and C. G. Kilsby, 2003: A regional frequency analysis of United Kingdom extreme rainfall from 1961 to 2000. *Int. J. Climatol.*, **23**, 1313–1334, https://doi.org/10.1002/joc.943.

Fu, S.-M., Y.-C. Zhang, H.-J. Wang, H. Tang, W.-L. Li, and J.-H. Sun, 2022: On the evolution of a long-lived mesoscale convective vortex that acted as a crucial condition for the extremely strong hourly precipitation in Zhengzhou. *J. Geophys. Res. Atmos.*, **127**, e2021JD036233, https://doi.org/10.1029/2021JD036233.

Galarneau, T. J., Jr., L. F. Bosart, and R. S. Schumacher, 2010: Predecessor rain events ahead of tropical cyclones. *Mon. Wea. Rev.*, **138**, 3272–3297, https://doi.org/10.1175/2010MWR3243.1.

Gu, X., Q. Zhang, V. P. Singh, L. Liu, and P. Shi, 2017: Spatiotemporal patterns of annual and seasonal precipitation extreme distributions across China and potential impact of tropical cyclones. *Int. J. Climatol.*, **37**, 3949–3962, https://doi.org/10.1002/joc.4969.

Hermanson, L., and Coauthors, 2022: WMO global annual to decadal climate update: A prediction for 2021–25. *Bull. Amer. Meteor. Soc.*, **103**, E1117–E1129, https://doi.org/10.1175/BAMS-D-20-0311.1.

Hersbach, H., and Coauthors, 2018a: ERA5 hourly data on pressure levels from 1940 to present. Copernicus Climate Change Service (C3S) Climate Data Store (CDS), accessed 4 August 2022, https://doi.org/10.24381/cds.bd0915c6.

——, and Coauthors, 2018b: ERA5 hourly data on single levels from 1940 to present. Copernicus Climate Change Service (C3S) Climate Data Store (CDS), accessed 4 August 2022, https://doi.org/10.24381/cds.adbb2d47.

Hill, K. A., and G. M. Lackmann, 2009: Influence of environmental humidity on tropical cyclone size. *Mon. Wea. Rev.*, **137**, 3294–3315, https://doi.org/10.1175/2009MWR2679.1.

Hlywiak, J., and D. S. Nolan, 2021: The response of the near-surface tropical cyclone wind field to inland surface roughness length and soil moisture content during and after landfall. *J. Atmos. Sci.*, **78**, 983–1000, https://doi.org/10.1175/JAS-D-20-0211.1.

Hoerling, M., and Coauthors, 2013: Anatomy of an extreme event. *J. Climate*, **26**, 2811–2832, https://doi.org/10.1175/JCLI-D-12-00270.1.

Jenkins, S., J. McAneney, C. Magill, and R. Blong, 2012: Regional ash fall hazard II: Asia-Pacific modelling results and implications. *Bull. Volcanol.*, **74**, 1713–1727, https://doi.org/10.1007/s00445-012-0628-7.

Jiang, H., J. B. Halverson, and J. Simpson, 2008: On the differences in storm rainfall from hurricanes Isidore and Lili. Part I: Satellite observations and rain potential. *Wea. Forecasting*, **23**, 29–43, https://doi.org/10.1175/2007WAF2005096.1.

Khouakhi, A., G. Villarini, and G. A. Vecchi, 2017: Contribution of tropical cyclones to rainfall at the global scale. *J. Climate*, **30**, 359–372, https://doi.org/10.1175/JCLI-D-16-0298.1.

Kimball, S. K., 2006: A modeling study of hurricane landfall in a dry environment. *Mon. Wea. Rev.*, **134**, 1901–1918, https://doi.org/10.1175/MWR3155.1.

Knapp, K. R., M. C. Kruk, D. H. Levinson, H. J. Diamond, and C. J. Neumann, 2010: The International Best Track Archive for Climate Stewardship (IBTrACS): Unifying tropical cyclone best track data. *Bull. Amer. Meteor. Soc.*, **91**, 363–376, https://doi.org/10.1175/2009BAMS2755.1.

——, H. J. Diamond, J. P. Kossin, M. C. Kruk, and C. J. Schreck, 2018: International Best Track Archive for Climate Stewardship (IBTrACS) Project, version 4. NOAA/National Centers for Environmental Information, accessed 1 January 2022, https://doi.org/10.25921/82ty-9e16.

Lai, Y., and Coauthors, 2020: Greater flood risks in response to slowdown of tropical cyclones over the coast of China. *Proc. Natl. Acad. Sci. USA*, **117**, 14 751–14 755, https://doi.org/10.1073/pnas.1918987117.

Li, F., Q. Wang, W. Hu, J. Liu, and X. Zhang, 2022: Rapid assessment of disaster damage and economic resilience in relation to the flooding in Zhengzhou, China in 2021. *Remote Sens. Lett.*, **13**, 651–662, https://doi.org/10.1080/2150704X.2022.2068987.

Brought to you by UNIVERSITY OF OXFORD-RADCLIFFE | Unauthenticated | Downloaded 09/18/23 11:06 AM UTC

Li, J., B. Liu, and J. Mao, 2021: Climatological intraseasonal oscillation in the middle–upper troposphere and its effect on the northward migration of the East Asian westerly jet and rain belt over eastern China. *Int. J. Climatol.*, **41**, 5084–5099, https://doi.org/10.1002/joc.7118.

Li, W., S. Zhao, Y. Chen, L. Wang, W. Hou, Y. Jiang, X. Zou, and S. Shi, 2022: State of China's climate in 2021. *Atmos. Oceanic Sci. Lett.*, **15**, 100211, https://doi.org/10.1016/j.aosl.2022.100211.

Luo, Y., and Y. Du, 2023: The roles of low-level jets in "21·7" Henan extremely persistent heavy rainfall event. *Adv. Atmos. Sci.*, **40**, 350–373, https://doi.org/10.1007/s00376-022-2026-1.

Mirhosseini, G., P. Srivastava, and L. Stefanova, 2013: The impact of climate change on rainfall Intensity–Duration–Frequency (IDF) curves in Alabama. *Reg. Environ. Change*, **13** (Suppl. 1), 25–33, https://doi.org/10.1007/s10113-012-0375-5.

Moore, B. J., 2010: Synoptic-scale environments and dynamical mechanisms associated with predecessor rain events ahead of tropical cyclones. M.S. thesis, Dept. of Atmospheric and Environmental Sciences, University at Albany, State University of New York, 150 pp., https://vlab.noaa.gov/web/albany-cstar/m.s.-theses.

——, L. F. Bosart, D. Keyser, and M. L. Jurewicz, 2013: Synoptic-scale environments of predecessor rain events occurring east of the Rocky Mountains in association with Atlantic basin tropical cyclones. *Mon. Wea. Rev.*, **141**, 1022–1047, https://doi.org/10.1175/MWR-D-12-00178.1.

Nie, Y., and J. Sun, 2022: Moisture sources and transport for extreme precipitation over Henan in July 2021. *Geophys. Res. Lett.*, **49**, e2021GL097446, https://doi.org/10.1029/2021GL097446.

Ntegeka, V., and P. Willems, 2008: Trends and multidecadal oscillations in rainfall extremes, based on a more than 100-year time series of 10 min rainfall intensities at Uccle, Belgium. *Water Resour. Res.*, **44**, W07402, https://doi.org/10.1029/2007WR006471.

O'Connell, D. R. H., 2005: Nonparametric Bayesian flood frequency estimation. *J. Hydrol.*, **313**, 79–96, https://doi.org/10.1016/j.jhydrol.2005.02.005.

Osetinsky-Tzidaki, I., and E. Fredj, 2022: The 50-and 100-year exceedance probabilities as new and convenient statistics for a frequency analysis of extreme events: An example of extreme precipitation in Israel. *Water*, **15**, 44, https://doi.org/10.3390/w15010044.

Overland, J. E., and M. Wang, 2021: The 2020 Siberian heat wave. *Int. J. Climatol.*, **41**, E2341–E2346, https://doi.org/10.1002/joc.6850.

Quesada-Román, A., J. A. Ballesteros-Cánovas, S. Granados-Bolaños, C. Birkel, and M. Stoffel, 2022: Improving regional flood risk assessment using flood frequency and dendrogeomorphic analyses in mountain catchments impacted by tropical cyclones. *Geomorphology*, **396**, 108000, https://doi.org/10.1016/j.geomorph.2021.108000.

Risser, M. D., and M. F. Wehner, 2017: Attributable human-induced changes in the likelihood and magnitude of the observed extreme precipitation during Hurricane Harvey. *Geophys. Res. Lett.*, **44**, 12 457–12 464, https://doi.org/10.1002/2017GL075888.

Schaller, N., and Coauthors, 2016: Human influence on climate in the 2014 southern England winter floods and their impacts. *Nat. Climate Change*, **6**, 627–634, https://doi.org/10.1038/nclimate2927.

Shen, W., I. Ginis, and R. E. Tuleya, 2002: A numerical investigation of land surface water on landfalling hurricanes. *J. Atmos. Sci.*, **59**, 789–802, https://doi.org/10.1175/1520-0469(2002)059<0789:ANIOLS>2.0.CO;2.

Stevenson, S. N., and R. S. Schumacher, 2014: A 10-year survey of extreme rainfall events in the central and eastern United States using gridded multisensor precipitation analyses. *Mon. Wea. Rev.*, **142**, 3147–3162, https://doi.org/10.1175/MWR-D-13-00345.1.

Utsumi, N., and H. Kim, 2022: Observed influence of anthropogenic climate change on tropical cyclone heavy rainfall. *Nat. Climate Change*, **12**, 436–440, https://doi.org/10.1038/s41558-022-01344-2.

Vasiliades, L., P. Galiatsatou, and A. Loukas, 2015: Nonstationary frequency analysis of annual maximum rainfall using climate covariates. *Water Resour. Manage.*, **29**, 339–358, https://doi.org/10.1007/s11269-014-0761-5.

Villarini, G., J. A. Smith, M. L. Baeck, T. Marchok, and G. A. Vecchi , 2011: Characterization of rainfall distribution and flooding associated with U.S. landfalling tropical cyclones: Analyses of Hurricanes Frances, Ivan, and Jeanne (2004). *J. Geophys. Res.*, **116**, D23116, https://doi.org/10.1029/2011JD016175.

——, R. Goska, J. A. Smith, and G. A. Vecchi, 2014: North Atlantic tropical cyclones and U.S. flooding. *Bull. Amer. Meteor. Soc.*, **95**, 1381–1388, https://doi.org/10.1175/BAMS-D-13-00060.1.

Wang, J., C. W. Yu, and S.-J. Cao, 2022: Urban development in the context of extreme flooding events. *Indoor Built Environ.*, **31**, 3–6, https://doi.org/10.1177/1420326X211048577.

Wu, Z., Y. Zhang, L. Zhang, H. Zheng, and X. Huang, 2022: A comparison of convective and stratiform precipitation microphysics of the record-breaking Typhoon In-Fa (2021). *Remote Sens.*, **14**, 344, https://doi.org/10.3390/rs14020344.

Xue, M., 2023: Preface to the special collection on the July 2021 Zhengzhou, Henan extreme rainfall event. *Adv. Atmos. Sci.*, **40**, 335–336, https://doi.org/10.1007/s00376-022-2018-1.

Yang, L., L. Wang, X. Li, and J. Gao, 2019: On the flood peak distributions over China. *Hydrol. Earth Syst. Sci.*, **23**, 5133–5149, https://doi.org/10.5194/hess-23-5133-2019.

——, G. Villarini, Z. Zeng, J. Smith, M. Liu, X. Li, L. Wang, and A. Hou, 2020: Riverine flooding and landfalling tropical cyclones over China. *Earth's Future*, **8**, e2019EF001451, https://doi.org/10.1029/2019EF001451.

Yang, S., B. Chen, F. Zhang, and Y. Hu, 2022: Characteristics and causes of extremely persistent heavy rainfall of Tropical Cyclone In-Fa (2021). *Atmosphere*, **13**, 398, https://doi.org/10.3390/atmos13030398.

Yin, J., H. Gu, X. Liang, M. Yu, J. Sun, Y. Xie, F. Li, and C. Wu,, 2022: A possible dynamic mechanism for rapid production of the extreme hourly rainfall in Zhengzhou City on 20 July 2021. *J. Meteor. Res.*, **36**, 6–25, https://doi.org/10.1007/s13351-022-1166-7.

Yin, L., F. Ping, J. Mao, and S. Jin, 2023: Analysis on precipitation efficiency of the "21.7" Henan extremely heavy rainfall event. *Adv. Atmos. Sci.*, **40**, 374–392, https://doi.org/10.1007/s00376-022-2054-x.

Yuan, J., D. Zhao, R. Yang, and H. Yang, 2018: Predecessor rain events over China's low-latitude highlands associated with Bay of Bengal tropical cyclones. *Climate Dyn.*, **50**, 825–843, https://doi.org/10.1007/s00382-017-3643-8.

Zeng, Z., C. Lai, Z. Wang, X. Chen, Z. Zhang, and X. Cheng, 2019: Intensity and spatial heterogeneity of design rainstorm under nonstationarity and stationarity hypothesis across mainland China. *Theor. Appl. Climatol.*, **138**, 1795–1808, https://doi.org/10.1007/s00704-019-02937-2.

Brought to you by UNIVERSITY OF OXFORD-RADCLIFFE | Unauthenticated | Downloaded 09/18/23 11:06 AM UTC

Zhang, G. H., and Coauthors, 2011: Spatial patterns of change trend in rainfall of China and the role of East Asia summer monsoon. *Arid Land Geogr.*, **34**, 34–42.

Zhang, S., Y. Chen, Y. Luo, B. Liu, G. Ren, T. Zhou, C. Martinez-Villalobos, and M. Chang, 2022: Revealing the circulation pattern most conducive to precipitation extremes in Henan province of North China. *Geophys. Res. Lett.*, **49**, e2022GL098034, https://doi.org/10.1029/2022GL098034.

Zhang, X. J., 2021: Influence of Typhoon "fireworks" on Shandong and its multi-mode test. *J. Agric. Catastrophol.*, **11**, 70–72.

Zhao, J., L. Chen, and D. Zhang, 2022: Characteristics and causes for the climate anomalies over China in summer 2021. *Meteor. Mon.*, **48**, 107–121, https://doi.org/10.7519/j.issn.1000-0526.2021.120201.

Zhou, C., K. Wang, and D. Qi, 2018: Attribution of the July 2016 extreme precipitation event over China's Wuhan. *Bull. Amer. Meteor. Soc.*, **99** (1), S107–S112, https://doi.org/10.1175/BAMS-D-17-0090.1.

Brought to you by UNIVERSITY OF OXFORD-RADCLIFFE | Unauthenticated | Downloaded 09/18/23 11:06 AM UTC